AIAA JOURNAL
Vol. 45, No. 10, October 2007

Zonal Detached Eddy Simulation of a Controlled Propulsive Jet

Nicolas Chauvet,* Sebastien Deck,† and Laurent Jacquin‡
ONERA, 92322 Châtillon Cedex, France

DOI: 10.2514/1.28562

This paper presents zonal detached-eddy simulation of a round underexpanded sonic jet exhausting from a realistic aircraft afterbody and controlled by four radial injections. The comparison with a former experiment proves the capability of zonal detached-eddy simulation to reproduce mean flow induced by the complex interaction between the compressible waves and the turbulent jet shear layer. However, the very near-field jet structure indicates that the shear-layer transition to a fully turbulent state is delayed. Therefore, a modification of the characteristic length scale used in the modeling is proposed which is shown to improve the prediction of the shear-layer growth. The control injectors are aimed to enhance jet mixing. Experiment indicated the efficiency of this additional device but also expressed the need for more data to get a deeper and more complete insight into the whole flowfield. Both spatial and temporal information are provided by zonal detached-eddy simulation which is then a good candidate. This method is shown to correctly simulate streamwise vortices generated by secondary injections, their action in jet distortion, as well as their subsequent decay. Finally, computational results allow us to evaluate the action of the hypermixer on turbulent activity and its consequences on jet dilution.

Nomenclature

a^*	=	critical speed of the primary flow
D	=	nozzle throat diameter
d	=	distance to the closest wall
k	=	turbulent kinetic energy
k^*	=	nondimensionalized turbulent kinetic energy integrated in jet cross sections (Y, Z)
M	=	Mach number
$\boldsymbol{N}$	=	normalized vorticity vector
p	=	pressure
$\langle p_i \vert p_{i0} \rangle$	=	nondimensionalized stagnation pressure averaged in the jet volume
Pr	=	Prandtl number
Q	=	mass flow rate
S_{ij}	=	components of the strain tensor
T	=	temperature
U	=	longitudinal velocity
$\boldsymbol{u}$	=	velocity vector
V_c	=	core volume
V_j	=	jet volume
X, Y, Z	=	Cartesian coordinates linked to the scale model
X, R, Θ	=	cylindrical coordinates
x, y, z	=	local coordinates linked to the grid cells
Δ	=	mesh characteristic length
$\Delta_{\max}$	=	Δ based on the maximum cell size
Δ_{vol}	=	Δ based on the cell volume
Δ_ω	=	Δ based on the vorticity
$\Delta x, \Delta y, \Delta z$	=	cell sizes in the local coordinate system
ϵ	=	small parameter
$\boldsymbol{\epsilon}$	=	small vector
μ	=	molecular dynamic viscosity
μ_t	=	turbulent dynamic viscosity
ν_t	=	turbulent kinematic viscosity
ρ	=	density
τ_{ij}^d	=	components of the deviatoric part of the Reynolds-averaged Navier–Stokes/subgrid-scale stress tensor
$\tau_{xr}^R, \tau_{xr}^{\text{RM}}, \tau_{xr}^{\text{RR}}$	=	total, modeled, and resolved Reynolds shear stress in the plane $(X;R)$
Ω_X	=	normalized streamwise vorticity $= \boldsymbol{\omega} \cdot \boldsymbol{x} D/(2a^*)$
$\boldsymbol{\omega}$	=	vorticity vector $= \boldsymbol{\nabla} \times \boldsymbol{u}$

Subscripts

i	=	isentropic stagnation value
0	=	ambient flow value
1	=	primary flow value
2	=	ventilation flow value
3	=	control flow value

Introduction

AERONAUTICAL applications and more generally many engineering issues are concerned with high Mach and Reynolds-number flows featuring attached and detached boundary layers in internal as well as external parts. Experiment has proved to be essential in the past while computational tools were still not mature, and is likely to remain as important in the future, not only to adjust or validate the numerical methods. Among its main drawbacks, experiment suffers from possible sidewall effects, the difficulty in respecting similitude laws (flight Reynolds numbers), and the dramatic cost induced by parametric variations on complex scale-model configurations. In principle, numerical simulations allow for arbitrarily defined flow conditions, and thus seem to be an attractive alternative for overcoming the previously mentioned shortcomings. However, complete simulation, also called direct numerical simulation (DNS), of industrial flows will not be feasible yet for many years because of the limitation in computing power required to reproduce the large range of turbulent scales [1]. On the other hand, Reynolds-averaged Navier–Stokes (RANS) simulations, supposed to model the time-averaged action of the whole turbulent dynamics on the mean flow, are low in cost and proved all the same to be accurate for predicting most of the attached boundary layers found in practical applications. Nonetheless, the most frequently used RANS models were shown to be deficient for complex shear flows involving strong compressibility, high temperatures, and three dimensionality as those encountered in propulsive jets [2,3]. Even if some dedicated models manage to reproduce the mean flow of

Received 26 October 2006; revision received 4 May 2007; accepted for publication 7 May 2007.

*Ph.D. Student, Applied Aerodynamics Department, 29 Avenue de la Division Leclerc; chauvet.nicolas@yahoo.fr.

†Research Scientist, Applied Aerodynamics Department, 29 Avenue de la Division Leclerc; sebastien.deck@onera.fr.

‡Head, Fundamental and Experimental Aerodynamics Department, 29 Avenue de la Division Leclerc; laurent.jacquin@onera.fr.

academic jets, their reliability for predicting new technological solutions remains questionable. For these kinds of flow, the only feasible methods at the present time are hybrid Reynolds-averaged Navier–Stokes/large-eddy simulation (RANS/LES) [4,5]. Their principle, in a practical view, is to explicitly compute the dynamics of all the turbulent eddies up to scales now affordable by computers, that is the flows detached from walls, and to be content with the time-averaged prediction of RANS methods in boundary layers. It is justified in detached flows where the small scales are expected to have a more universal behavior than the large ones, and therefore supposed to be easier to model. In high-Reynolds-number flows where most of the kinetic energy is brought by the largest scales, this approach showed very fair results on the mean flow as well as on unsteady data. The most commonly used hybrid technique is probably the detached-eddy simulation (DES) originally proposed by Spalart et al. [6]. Among the successful or encouraging applications of this method, we can mention turbulent flows over various solid bodies like a backward-facing step and an aircraft landing gear truck [7], a sphere [8], and an F-15E at a 65-deg angle of attack [9].

In the framework of a research program on the alleviation of the infrared signature of propulsive jets, an experiment [10] on the mixing properties of underexpanded jets controlled by steady radial injections has been conducted in the S3Ch wind tunnel at ONERA. This means of control was already tested by Davis [11] who highlighted its mixing capability in an academic round jet. Later, Collin et al. [12] took a closer look at the interaction between one secondary jet and the shear layer of the primary jet. They evidenced an unsteady penetration process responsible for a local boost in the turbulence of the shear layer which is yet rapidly damped downstream. The aim of the research program was to test the feasibility of radial injections for enhancing the mixing of a realistic combat-aircraft propulsive jet. The stagnation pressure measured on the axis of the jet controlled by four injections indicated a net reduction in the potential core length. In addition, tomoscopic photographs highlighted a strong alteration of the jet boundary. Moreover, Schlieren visualizations exhibit a thorough modification of the internal shock/wave structure. All the measurements then proved the action of radial blowing on a realistic jet. They also expressed the need for collecting much more extended data of the flowfield in order, first, to have a deeper understanding of the physical mechanisms activated by secondary jets, and second, to get a better estimation of the mixing efficiency. As a first numerical investigation, RANS simulations were carried out [13]. They permitted showing that the internal shock/wave modification, though impressive due to the strong jet distortion, cannot generate such a steady shear sufficient to be in charge of the global mixing enhancement. Furthermore, global measures of mixing were computed in several configurations and a parametric study indicated the result of some control variations on jet mixing. Nevertheless, RANS flowfields displayed some discrepancies with the experimental data. These discrepancies have motivated the use of a more accurate state-of-the-art simulation for the applied configuration, namely zonal-detached-eddy simulation [14,15] (ZDES), which is the subject of this article. To the authors' knowledge, few studies dealing with DES-type simulation of jet shear layers have been published. Shur et al. [5,16,17] aiming at predicting the noise radiated from jets of airliner engines, presented a zonal hybrid RANS/LES methodology able to fairly satisfy their expectations. The computation was conducted in two steps. In the first stage, the boundary layers were calculated by a RANS approach. In the second stage, the obtained eddy-viscosity field was then imposed in the boundary layers of the LES calculation. The grids in these areas were also made coarser. In addition, the eddy viscosity was set to zero in the jet volume to effectively perform an implicit LES. The methodology employed herein strives to reduce the user's intervention even if special care is still required to build the mesh as for any LES, and that the switch from the RANS mode to the LES one is performed explicitly according to the zonal approach [15], this latter user intervention being straightforward in the case of a jet exhausting from a nozzle.

The paper is organized in four parts as follows. First, test cases are described to emphasize the geometrical and physical complexity of this "industrial" propulsive jet [5] as opposed to "academic" ones. Second, the numerical method comprising the ZDES approach is detailed and the meshing choices are explained. As it will be shown later, flowfields predicted by this basic method make significant improvements over RANS computations from 3 throat-diameters D downstream of the primary nozzle. However, initial shear-layer growth is underpredicted by this basic method. To overcome this drawback, a modification of the characteristic length scale Δ used by the hybrid method is proposed in a third part. Then, the computed flowfields are compared with previous measurements and RANS results. The benefit of the new Δ definition is highlighted and analyzed. Finally, the efficiency of the mixing device is assessed thanks to turbulent stresses and mean flow quantities available in the whole computational field.

Test Cases

Experimental Setup

To get acquainted with the jet controlled by radial injections, an experiment was undertaken in cold flows. The presented simulations have the ambition to reproduce two test cases with and without control. No extrapolation will be made to real hot jet mixing. The experiment was carried out in the S3Ch continuous research wind tunnel of ONERA's Chalais Meudon center. The test section is square shaped, and the dimensions of the test chamber are 0.78×0.78 m^2. The apparatus displayed in Fig. 1a is based on a representative combat-aircraft afterbody delivering a primary sonic jet surrounded by an annular secondary flow for ventilation. It is mounted on a profiled sting. The different streams around the afterbody are depicted in Fig. 1b. The far-field conditions of the external stream are $M_0 = 0.8$ for the Mach number and $p_0 = 0.66hPa$ for static pressure. The primary jet is completely characterized by its stagnation conditions $T_{i1} = 300$ K and $p_{i1} = \text{NPR} \times p_0$. Two nozzle pressure ratios (NPR) were tested corresponding, respectively, to the cruise regime (NPR = 3.1) and to the full-throttle one (NPR = 5.0). Both regimes are described in [18] but only the mild underexpansion ratio is simulated here. The ventilation stream is determined by its total temperature $T_{i2} = 270$ K and its mass flow rate $Q_2 = 22$ g/s. Several fluidic control devices were tested. They consist in eight radial sonic injectors. An arbitrary number of these injectors can be activated. Both measurements [10] and preliminary RANS computations [13] showed that the activation of four injectors (one out of two injectors) dramatically alters the jet flow. Then, the four-active-injector configuration was chosen as the controlled-jet case. The injected air is cold $T_{i3} = 300$ K and the mass flow rate is $Q_3 = 26$ g/s. The flow field has been characterized by

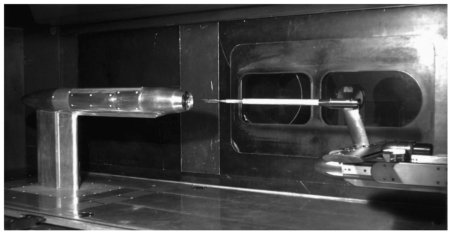

a) Afterbody mounted on the profiled sting

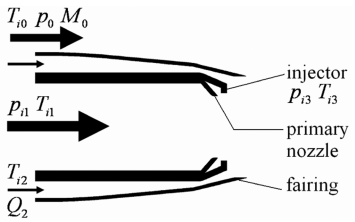

b) Sketch of the afterbody

Fig. 1 Experimental setup.

means of Schlieren visualizations, tomoscopic pictures, pressure and temperature measurements, as well as two-component particle imaging velocimetry (PIV) (for the no-control case only). A complete description of the experiment is available in [10]. The Mach number spreads from 0.02 in the ventilation to 1.8 upstream from the first shock while the fully expanded jet Mach number is $M_j = 1.38$. At the very beginning of the shear layer, the calculated convective Mach number M_c [19,20] between the fully expanded jet condition and the ventilation stream ($M \approx 0$, p_0) is 0.64 and it tends to 0.23 as the jet progresses into the external coflow ($M_0 = 0.8$, p_0). These calculated values are in fact the upper bounds of the convective Mach number, as they do not include the action of mixing.

Mesh Description

The design of a hybrid RANS/LES grid is of paramount importance because it can, if it is not built with care, lead to unphysical results. The basic geometry of the experimental scale model was reproduced. Preliminary RANS computations [13] not presented in this paper indicated some crucial points which have to be taken into account. They emphasized in particular the sensitivity of the jet shock structure to the external boundary-layer thickness. This latter one determines the spatial distribution of the momentum of the external flow which impacts the jet boundary and in that way alters the pressure on it. It was thus decided to calculate the boundary layer along a cylindrical wall representative of the whole sting. In addition, those RANS calculations showed that an orthogonal mesh is necessary to properly capture the underexpanded jet shock structure on the jet axis. The computational domain used for both cases, with and without control, extends over $12D$ (D being the throat diameter) in the radial direction and over, respectively, $18D$ upstream and $25D$ downstream of the nozzle throat. However, the finest mesh covers only the maximum area probed during the experiment, that is, $9D$ downstream of the nozzle. Because of the code formulation, each one of the 31 blocks of the computational field is made of structured hexahedral cells. Therefore, the challenge was to build a structured mesh which combines RANS requirements for the attached boundary layers, grid clustering close to geometric singularities, that is, solid injectors and secondary jets, as well as a homogeneous grid to fulfill the LES conditions [21]. A cutaway view through the mesh around the afterbody is displayed in Fig. 2, and Fig. 3 shows plane views in transverse and longitudinal cross sections. The flow in the jet core is discretized by means of a O–H block topology to properly capture the shock reflections on the axis. The boundary layers inside the primary nozzle and along the external fairing include 25 points and have, respectively, a first node at constant $\Delta r = 2.3 \times 10^{-5}D$ and $4.5 \times 10^{-5}D$ from the wall that is $y^+ = 0.5$ in wall units at the nozzle lip and $y^+ = 0.8$ on the outer wall. The volume occupied by the jet from the nozzle throat in both cases, control on and off, is discretized in 236 nodes in the longitudinal direction and 172 nodes in the radial one. To assess the effect of the grid refinement in the circumferential direction, two meshes had been built. A first mesh denoted M1 of 8.0×10^6 nodes comprises 129 points in azimuth and a second one denoted M2 of approximately 10.5×10^6 nodes has 169 points in azimuth. The large number of nodes in the radial direction, due to the node propagation from the boundary layers, is necessary to cover the strongly distorted jet shear layer in the controlled case [13,18]. Without control, the jet only spreads on 100 cells in the radial direction. No special refinement was performed around the first shock for four reasons: 1) RANS grid convergence was reached with this longitudinal discretization; 2) the grid distribution adapted to the growth of the jet shear layer is fine enough, leading to $1.6 \times 10^{-2}D$-long cells on the shock, this latter one being smeared on three cells; 3) the mesh was originally thought to support several simulations with different underexpansion ratios, hence different shock positions; 4) this spatial discretization is expected to be sufficient to reproduce the influence of the shock on the resolved scales of the mixing layer, the contribution of the purely inviscid shock interaction being negligible according to a previous study [13]. Moreover, as the mesh is structured and the shocks propagate radially in the downstream direction, a dedicated shock refinement would have resulted in an excessive addition of nodes. This is all the more true as the unsteady shock moves along an a priori unknown spatial range. With regard to the injections, we preferred to mesh the control-jet nozzles to correctly reproduce their exit flow rather than employ boundary conditions. The exit area of each one of the control jets is patched by

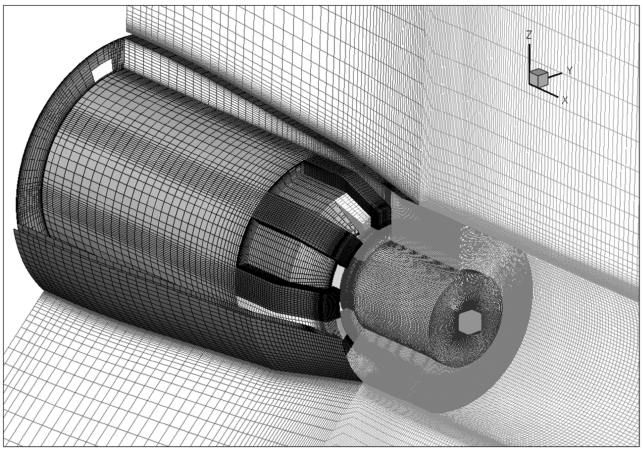

Fig. 2 Cutaway through the 3-D mesh M2 around the afterbody.

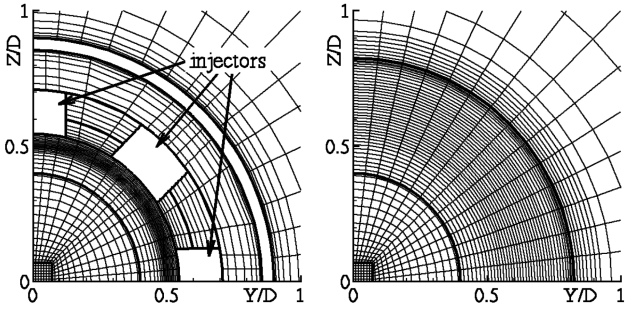

a) Transverse cross sections through the injectors (left) and further downstream at X/D=0.6 (right)

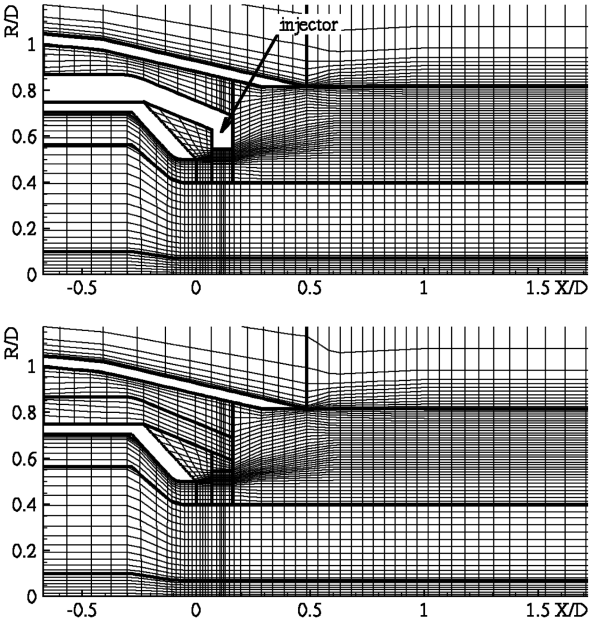

b) Longitudinal cross sections in the plane of injection (top) and in the plane between injectors (bottom)

Fig. 3 Mesh details in several characteristic cross sections (one every third cell is plotted).

60 cells whose size is $6 \times 10^{-3} D$. The solution computed on the finest grid M2 is discussed herein. The influence of the grid on the numerical result will be discussed in a devoted section.

Numerical Method

General Description

Simulations were performed with the FLU3M code developed by ONERA. It solves the Navier–Stokes equations on multiblock structured grids. The Navier–Stokes equations are discretized using a second-order finite-volume scheme on a cell-centered stencil. Roe's flux difference splitting is employed for the advective fluxes, MUSCL approach extends the spatial accuracy to the third order (3rd-order upwind-biased) and is combined with the Jameson's sensor to satisfy TVD conditions on shocks. Harten's correction with a coefficient equal to 10^{-4} is employed to avoid a wrong behavior of entropy. All viscous terms are centrally differenced. Time integration is based on second-order accurate Gear's formulation [22,23] and the inversion of the implicit system is performed by means of a lower–upper symmetric-Gauss–Seidel (LU-SGS) factorization. Owing to the approximations done in the implicit stage, Pulliam's inner-iteration algorithm was implemented to restore time accuracy. More details concerning the numerical method and implementation of turbulence models can be found in [23,24]. This well-tried solver has been notably used to compute a LES of the flow over a cavity at high-Reynolds number [25], a zonal DES of transonic buffet over a supercritical airfoil [14], a zonal DES of the flow around a high-lift configuration [15], several hybrid RANS/LES of supersonic base flows [26], and LES of a synthetic jet in a crossflow [27].

Zonal Detached-Eddy Simulation

The original detached-eddy simulation due to Spalart et al. [6] and denoted DES97 in this article is based on the Spalart–Allmaras RANS model. Here, we briefly mention its salient features necessary for the present flow configuration and refer to the original papers [28,29] for a full description. This empirical model is based on the transport equation of a quantity $\tilde{\nu}$ equal to the eddy viscosity ν_t except in the buffer and viscous layers:

$$\frac{D\rho\tilde{\nu}}{Dt} = \underbrace{c_{b1}\tilde{S}\rho\tilde{\nu}}_{\text{production}} + \underbrace{\frac{1}{\sigma}[\boldsymbol{\nabla}\cdot((\mu+\rho\tilde{\nu})\boldsymbol{\nabla}\tilde{\nu}) + c_{b2}\rho(\boldsymbol{\nabla}\tilde{\nu})^2]}_{\text{diffusion}} - \underbrace{\rho c_{w1} f_w \left(\frac{\tilde{\nu}}{d}\right)^2}_{\text{destruction}} \tag{1}$$

$$\tilde{S} = \|\boldsymbol{\omega}\| + \frac{\tilde{\nu}}{\kappa^2 d^2} f_{v2}, \qquad \boldsymbol{\omega} = \boldsymbol{\nabla}\times\boldsymbol{u} \tag{2}$$

The quantity $\tilde{S}$ equals $S = \|\boldsymbol{\omega}\|$ except in the buffer and viscous layers. The eddy viscosity is then defined as $\nu_t = f_{v1}\tilde{\nu}$. The production and diffusion terms are calibrated in a way to reproduce free shear flows, whereas functions f_{v1}, f_{v2}, and f_w are near-wall corrections. The idea suggested by Spalart et al. [6] was to modify the destruction term so that the RANS model is reduced to a LES subgrid-scale one in the detached flows. They proposed to replace the distance d to the closest wall with $\tilde{d}$ defined by

$$\tilde{d} = \min(d, C_{\text{DES}}\Delta) \tag{3}$$

where Δ is a characteristic mesh length. Away from the wall, if the destruction term balances the production one, the eddy viscosity scales with the length Δ and the local vorticity modulus S: $\nu_t \sim S\Delta^2$, then adopts the form of Smagorinsky's subgrid-scale (SGS) viscosity $\nu_{\text{SGS}} \sim \sqrt{2S_{ij}S_{ij}}\Delta^2$, where S_{ij} are the components of the strain tensor. Moreover, the subgrid model behaves somewhat like a dynamic model because of the material derivative and the diffusion term. Originally, the authors chose to define Δ as the largest of the spacing in all three directions

$$\Delta = \Delta_{\max} = \max(\Delta x, \Delta y, \Delta z) \tag{4}$$

so that the model "naturally" switches from the RANS behavior in the grid region typical of a boundary layer, that is $d \ll \Delta = \max(\Delta x, \Delta z)$ ($\boldsymbol{y}$ being normal to the wall) to the LES behavior away from the wall, that is $\Delta \ll d$. Nevertheless, and from the beginning, a special concern was devoted to the region, named "gray area," where the model switches, and where the velocity fluctuations, the "LES content," are expected to be not sufficiently developed to compensate for the loss of modeled turbulent stresses. This can lead to unphysical outcomes, like an underestimation of the skin friction, and then motivated, first, the publication of an educational paper [30] to specify the peculiarity of DES97 meshes, then, a modification of $\tilde{d}$, presented as a delayed DES [31], to extend the RANS mode and prevent "modeled-stress depletion." To get rid of this drawback, Deck [14,15] proposed a zonal approach of the original DES, called zonal-DES or ZDES, in which RANS and (DES) domains are selected individually. Figure 4 shows the zonal splitting adopted in the present computational domain. In RANS regions, the model is forced to behave as a RANS model, whereas in (DES) regions, the model can switch from the RANS mode to the LES mode by means of (3). The zonal approach is well adapted to treat free shear flows. Its advantage is that the user can focus his grid refinements on the regions of interest without corrupting the boundary-layer properties farther upstream or downstream. For instance, in (DES) regions, the grid is designed to obtain nearly cubic cells. In these regions, Deck also suggested to adopt the classical characteristic length scale used in LES and based on the cell volume:

$$\Delta = \Delta_{\text{vol}} = (\Delta_x\Delta_y\Delta_z)^{1/3} \tag{5}$$

In addition, the near-wall functions of the RANS model are explicitly disabled in the LES mode of (DES) regions (but not in the RANS mode) as follows [32]:

$$f_{v1} = 1, \qquad f_{v2} = 0, \qquad f_w = 1 \tag{6}$$

This choice avoids the low-eddy-viscosity levels typical of resolved LES regions being treated like in boundary layers. The use of (5) and (6) in (DES) regions justifies that its notation is distinguished from DES97. In practice, (DES) switches very quickly to the LES mode thanks to (5) and (6). In this way, the LES mode is managed by the transport equation of ν_t calibrated for free shear flows plus a destruction term rescaling the subgrid-scale viscosity in function of the mesh resolution. To complete the closure of RANS/SGS stress tensor, its deviatoric part is linearly linked to the deviatoric part of the resolved strain tensor:

$$\tau_{ij}^d = 2\rho\nu_t(S_{ij} - \tfrac{1}{3}S_{ll}\delta_{ij}) \tag{7}$$

whereas its isotropic part which trace equals $\frac{2}{3}$ times the specific kinetic energy (of the whole of the turbulence in RANS mode or under the gridscale in LES mode) can be included in the pressure term and is often neglected with respect to this latter one. This choice was adopted for the present work. The RANS or subgrid heat flux is modeled by a Fourier's law and a constant Prandtl number $Pr_t = 0.9$.

Modification of the Mesh Characteristic Length Δ

Motivation

The application of large-eddy simulation on structured hexahedral grids requires that the cells are as much as possible cubic. However, it is unrealistic to discretize practical engineering flows, in particular axisymmetric turboreactor nozzles fitted with chevrons, lobes, or microfluidic-actuators, in nearly cubic meshes. The grid anisotropy should then be taken into account in the definition of the SGS viscosity. It is worth remembering that a modification of the SGS viscosity has no influence on the resolution of the boundary layers here thanks to the zonal approach. Several methods were developed and are reviewed in [33]. A straightforward means of considering the anisotropy in the SGS viscosity is to directly modify the mesh characteristic length Δ. The most widely used model in LES is the

one proposed by Deardorff [34] and adopted by Deck for the zonal-DES [15], Δ_{vol}. Extensions of Deardoff's proposal include the length-scale chosen for the original DES [6], $\Delta_{\max}$, and another one defined by

$$\Delta = \sqrt{(\Delta_x^2 + \Delta_y^2 + \Delta_z^2)/3} \tag{8}$$

Scotti et al. [35] also proposed a definition of Δ based on the estimation of the dissipation rate of an isotropic turbulence in anisotropic grids. At the very beginning of the jet shear layer, the cell sizes are subject to a strong anisotropy due to the dense grid distribution coming from the boundary layer as well as an inhomogeneity due to the refinement around the injectors. All the existing definitions of Δ known by the authors depend on the cell size in the spanwise direction of the shear layer. In the present mesh, this induces an azimuthal variation of the SGS viscosity which is physically unjustified. In the more general frame of the shear-layer calculation, this dependence of the solution on the arbitrary set spanwise cell length is untenable. Because in practical applications, especially in axisymmetric shear layers, this length is much larger than both the other ones, classical Δ definitions lead to an excessive modeled viscosity. In the jet shear layer computed with Δ_{vol} described in the following section, it will be shown that the destabilization and creation of vortical structures are delayed, which supports the above remarks. From both the strong anisotropy and inhomogeneity aspects arose the need to create a Δ definition which cuts this dependence with respect to the shear-layer spanwise mesh length by introducing a flow-dependent definition.

Formulation

In a plane shear layer, whose spanwise direction is $\boldsymbol{z}$, the above-mentioned demand is translated into a dependence of Δ on Δ_x and Δ_y only; for example:

$$\Delta = \sqrt{\Delta_x \Delta_y} \tag{9}$$

In an arbitrarily oriented shear layer, the need for a Galilean-invariant definition dismisses a direct use of the velocity component, but allows the one of its spatial derivatives. Vorticity $\boldsymbol{\omega}$ is a straightforward vector quantity to point the local spanwise direction of the shear layer. Then, the new expression of Δ was proposed as follows:

$$\boldsymbol{\epsilon} = \frac{\epsilon}{\sqrt{3}}(\boldsymbol{x} + \boldsymbol{y} + \boldsymbol{z}); \qquad \boldsymbol{N} = \frac{\boldsymbol{\omega} + \boldsymbol{\epsilon}}{\|\boldsymbol{\omega} + \boldsymbol{\epsilon}\|} \tag{10}$$

$$\Delta = \Delta_\omega = \sqrt{N_x^2 \Delta_y \Delta_z + N_y^2 \Delta_z \Delta_x + N_z^2 \Delta_x \Delta_y} \tag{11}$$

The unit vector $\boldsymbol{N}$ which local components are (N_x, N_y, N_z) gives the orientation of $\boldsymbol{\omega}$. ϵ is a small value that stands for preventing zero divide when the vorticity vanishes. A value of $\epsilon = 10^{-8}$ was chosen in the present computations. As explained above, the new definition was initially motivated to prevent a delayed development of instabilities in the shear layer and a subsequent late transition to a fully turbulent flow. We will now see how it behaves in actually turbulent flows.

Discussion of the New Definition for Turbulent Flows

In an isotropic mesh, $\Delta_x = \Delta_y = \Delta_z$, it is easy to check that all the Δ definitions degenerate into $\Delta_{\max} = \Delta_{\text{vol}} = \Delta_\omega = \Delta_x$. Concerning the constant C_{DES}, it was calibrated for an isotropic homogeneous turbulence [36] in an isotropic Cartesian mesh for which $\Delta_\omega = \Delta_{\max}$, therefore no readjustment is necessary. Independently from the value of the vorticity, it can also be found that Δ_ω admits the following lower and upper bounds:

$$\min_{\alpha \neq \beta}\left(\sqrt{\Delta_\alpha \Delta_\beta}\right) \leq \Delta_\omega \leq \max_{\alpha \neq \beta}\left(\sqrt{\Delta_\alpha \Delta_\beta}\right) \tag{12}$$

Contrary to the definitions seen above, Δ_ω is flow dependent. More precisely, it introduces the notion that at any spatiotemporal point, if the vorticity is not zero, there exists one particular direction indicated by the vorticity $\boldsymbol{\omega}$. Considering a local vortex whose spin axis is $\boldsymbol{N}$, the rotating motion is captured by the mesh only if the grid resolution is fine enough in the plane normal to $\boldsymbol{N}$. At this point and in this vorticity direction, the mesh lengths in this plane determine the minimum vortex scale aligned on $\boldsymbol{N}$ that can be resolved and are then intuitively the characteristic lengths that should be taken into account in the subgrid stresses, and so included in the Δ definition. As turbulence is unsteady and 3-D by nature, $\boldsymbol{N}$, at a given position, changes in time and then designates two other characteristic lengths at each instant.

Results and Discussion

Computational Description

The stagnation conditions (p_i, T_i) of the primary jet and the control injections measured experimentally were imposed in the computational models. As only the stagnation temperature and the total mass flow rate were available for the ventilation stream, a subsonic mass flow rate was applied as an inlet condition. The ventilation inlet geometry is also representative of the scale model: the stream enters the annular channel by four holes whose cross-section area is 6% of the total area of the channel. One of these holes is shown in Fig. 2. The computations were performed without any artificial excitation and yet showed that the shear layer was able to develop a growing instability leading to an apparent (partially resolved) turbulent jet. Based on the work of Wallace and Redekopp [37], it was previously suggested [10] that the jet-wake profile induced by the low-speed ventilation coflow could sustain an absolute instability. A further analysis should be undertaken to confirm this assumption. Numerical noise or initial transients can also trigger convective instabilities in the jet shear layer. Another ZDES simulation was conducted with the help of $\Delta_{\max}$ definition of the original DES and the same numerical scheme as the one described above. The resulting jet shear layer turned out to hardly destabilize and no turbulent eddies could be detected. In other words, the standard DES almost damps the development of the instabilities in the shear layer. This reveals that the eddy viscosity that scales on $\Delta_{\max}$ is too large. Indeed, values of μ_t/μ greater than 120 were probed in the near field. The cases control on and off were then computed with Δ_{vol} and Δ_ω and are, respectively, referred to as ZDES1 and ZDES2 in the following.

Each case was computed in three steps. First, a RANS calculation was carried out with the Spalart–Allmaras turbulence model [28,29], which is widely used in complex compressible flows [38,39]. As the streamwise vorticity plays a role in the present flows, the rotational correction of this model [40] was used to limit excessive turbulent diffusion in the vortex cores. RANS simulation were fully iteratively converged to steady state on both grids presented above which proved their grid convergence. A detailed description of these computations and the resulting steady flows were thoroughly discussed in a former paper [13]. These ones are used to initialize the ZDES calculations. For these latter, the rotational correction of the RANS model was deactivated, as most of the turbulent dynamics is then expected to be explicitly resolved. A transient stage lasted approximately $80 \cdot T_c$ before the fully developed turbulent flow could reach a statistically steady state. The characteristic timescale is defined by $T_c = D/a^*$, with D the throat diameter and a^* the critical speed. Then, statistics of first and second order were collected during $150 \cdot T_c = 20$ ms. This length of the statistical sampling window is sufficient because the time-averaging process was extended to $900 \cdot T_c = 120$ ms and showed no significant changes in the results presented herein. This longer duration was necessary to perform a proper study of the spectral properties of the fluctuating field which will be the subject of a future paper. The CPU cost per cell and per inner-iteration is less than 1 μs. The simulations are performed on a single processor of a NEC-SX6 supercomputer running approximately at 4 Gflops. A time step of $\Delta t_{\text{CFD}} = 1$ μs, or $\Delta \tilde{t} = \Delta t / T_c = 7 \times 10^{-3}$, leading to a maximum CFL number based

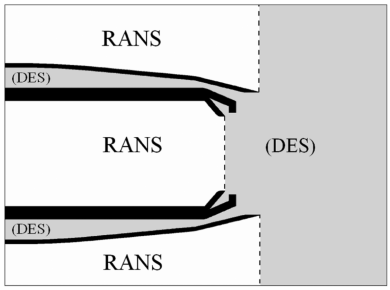

Fig. 4 RANS regions and (DES) regions in the computational field.

on the maximum acoustic velocity $(u + a)$ of $\mathrm{CFL}_{\max} = 13$, is computed with 5 inner iterations to meet the temporal accuracy. The convergence of the inner-iteration process was checked to reach a drop of at least one order in the residuals.

Jet Shock Structure

Figure 5 shows horizontal-knife Schlieren pictures (vertical density gradient) of the mean flow in uncontrolled and controlled jets extracted from experiment, RANS calculations, and both ZDES (from top to bottom). Each reference jet is displayed on the left side of the figure. The jet axis is $(O, \boldsymbol{X})$, (X, Y, Z) denotes the Cartesian frame linked to the scale-model, and (X, R, Θ) denotes the cylindrical frame. We call "injection-plane," a longitudinal plane (X, R) crossing two opposite blowing injectors, and "interplane," the one between two active injectors. The experimental photograph of the control jet was made in the direction normal to the injection-plane (X, Z). For the simulations, pictures located in the center of Fig. 5 are in an injection plane, whereas the ones on the right side are in an interplane.

In the experimental reference jet (no control), one can notice a shock with a lens shape which is characteristic of mildly underexpanded sonic jets. In the particular configuration studied here, this shock was seen to be extremely sensitive to the growth of the jet shear layer. Therefore, even though no information is available

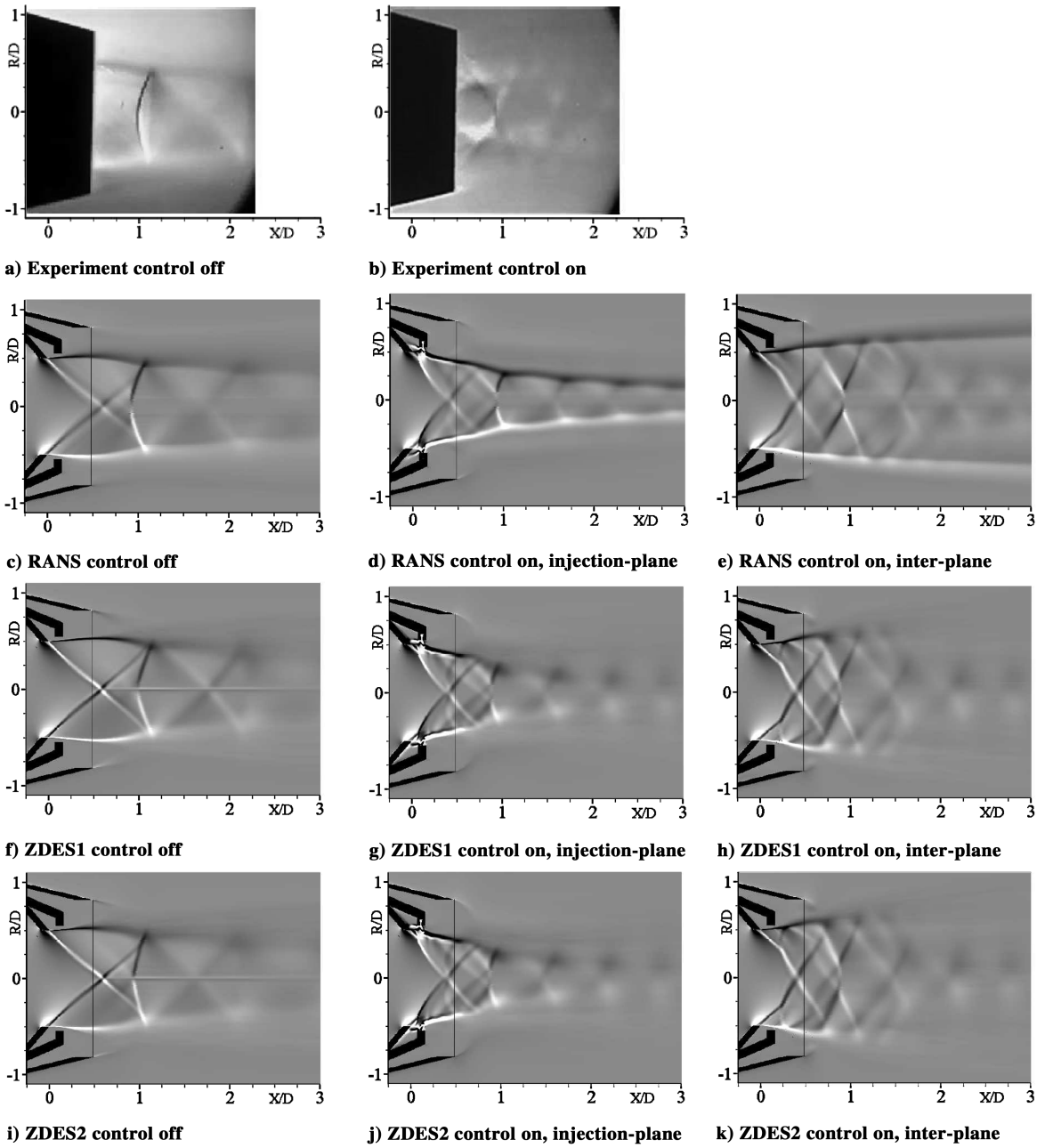

Fig. 5 Schlieren visualizations of the uncontrolled and controlled jets (grid M2).

from experiment before $X/D = 0.5$ due to the obstruction of the external fairing, we considered that a simulation properly reproduces the initial shear layer if this shock lens has a shape similar to the one observed in the experiment and if its axial position is correct. Further examination reveals that the shear-layer thickness influences the confluence of the ventilation and external coflows more precisely the topology of their streamlines, and then the pressure distribution on the jet boundary, leading to a modification of the inner-wave reflection and shock structure. RANS computations give the thicker shear layer up to the shock while ZDES1 provides the thinner one. ZDES2 exhibits a shear-layer thickness close to the one of ZDES1 up to the end of the external fairing, at $X/D = 0.5$, then a rapidly growing shear layer rather close to the one of RANS simulation. As a consequence, we can observe that, in ZDES1, the shock lens occurs slightly downstream of what is predicted in RANS and ZDES2. In all the computed flowfields, we can see an axisymmetric wave originating from the nozzle lip due to the wave reflection on the flat portion of the throat. This conical wave is so steep on the axis in ZDES flows that it forms an infinitesimal Mach disk [41] and a subsequent higher entropy stream tube visible by the resulting cross-stream density gradient. This assertion was verified by a survey of the total pressure field not shown here. This feature, not visible in the experimental photograph, is not intended to have a significant influence on the whole flow because the total pressure defect is weak and very localized. When the control is on, the bow shocks, coming from the secondary-jets obstruction, intercept these waves and prevent the formation of the small Mach disk. All predicted flows also show the expansion-compression pattern typical of imperfectly expanded supersonic jets.

In the controlled case, all of the computations reproduce the diamond-shaped shock structure visible in the experiment. Nonetheless, ZDES results show weaker waves not captured by the RANS method. These latter ones cannot be precisely identified in the experiment because of the highly 3-D character of the flow. Contrary to what was seen in the reference jet, no difference is noticed between the two ZDES when control is activated. RANS and ZDES fields can be distinguished by their gradients in the shear layer from approximately the impact region of the internal shock at $X/D \approx 0.75$. These gradients appear as very steep in RANS flow, whereas they are completely diffused in both ZDES. This fact lets us think of enhanced turbulent exchanges and then diffusion and dissipation in the ZDES-predicted shear layers. Because of more persistent gradients in the shear layer, RANS pictures highlight a sustained jet distortion.

Figure 6 displays the corresponding instantaneous horizontal-knife Schlieren views from experiment, and numerical Schlieren planes extracted from ZDES1 and ZDES2. The experimental pictures highlight the turbulent nature of the investigated flow. Yet, the shock lens of the reference jet (Fig. 6a) does not seem to be significantly disturbed. When the radial injections blow (Fig. 6b), the jet flow seems to spread in the radial direction and the wake of the injections normal to the plane of the figure is hardly discernible. As for the numerical results, in the reference case (Figs. 6c and 6f), one can see that the shear-layer destabilization is delayed in ZDES1. That was one of the reasons for the new Δ definition. As a result, we can notice the early development of instabilities in the shear layer of ZDES2. These are also emphasized by highly unsteady supersonic waves emanating from the distorted shape of the shear layer. These waves impacting the shock lens create entropy radial stratifications laying on the flow trajectories and visible through density streaks. The wave structure is also not the same downstream from the first shock. A striking feature highlighted by these views is the stability of the position and shape of the shock compared to the strongly fluctuating shear layer.

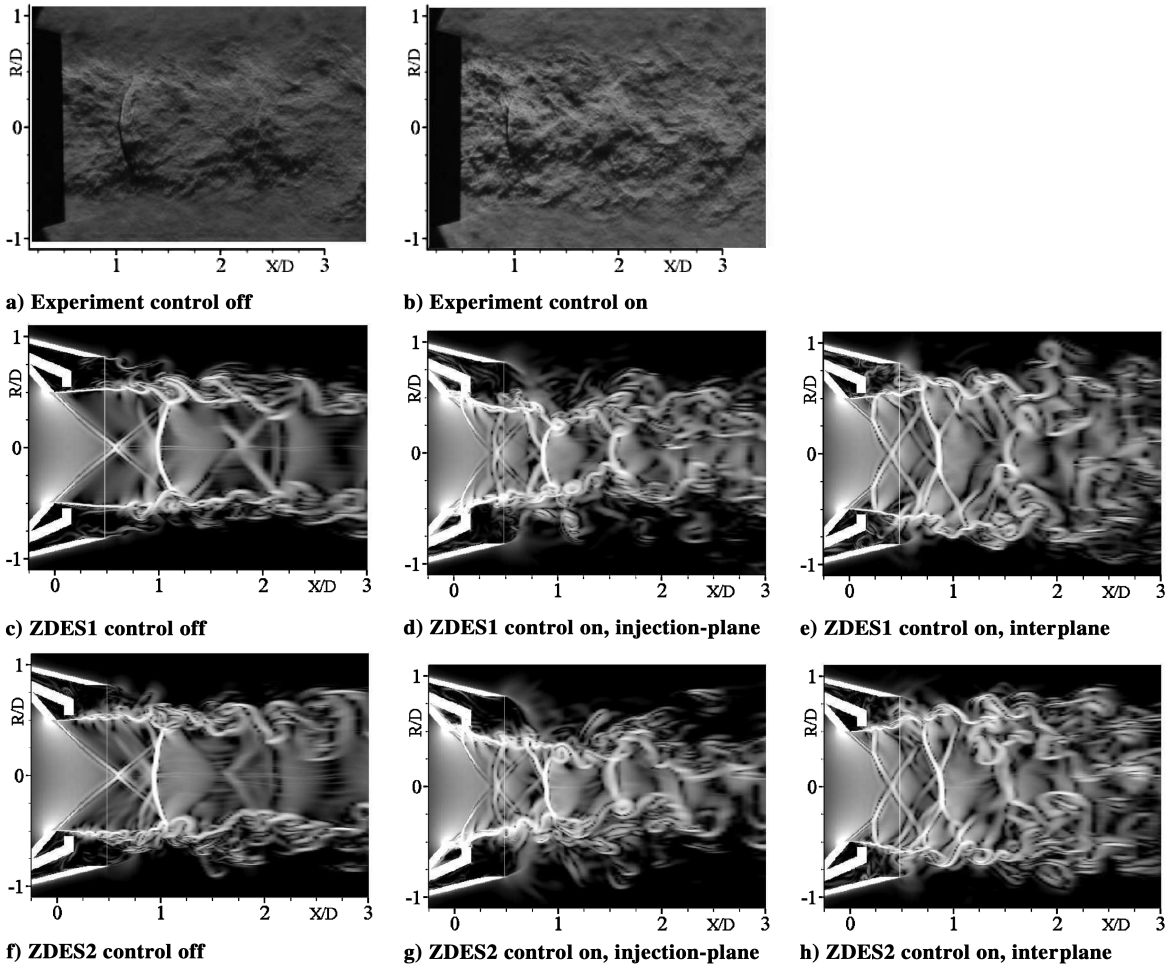

Fig. 6 Instantaneous Schlieren of the uncontrolled and controlled jets (grid M2).

When the radial injections are activated (pictures in the center and right side of Fig. 6), the organization and location of the turbulent eddies drastically change, these ones penetrating more deeply into the jet (Figs. 6d and 6g) and expanding farther away from the axis in the interplanes (Figs. 6e and 6h). From this, one may expect a shortening of the potential core as well as an increased jet expansion and diffusion by the large spreading of turbulent exchange area. Even if the increased area does not enhance the mixing as claimed by Zaman [42], it probably allows a larger number of eddies to entrain the external fluid into the jet. Consequently, to the jet distortion, shock waves are seen to be more disturbed than in the no-control jet. The highly 3-D aspect of this flow is emphasized by the numerical visualizations in planes with active and inactive injections. This indicates that any precise physical interpretation of the experimental Schlieren visualization, Fig. 6b, is tricky and justifies resorting to numerical investigations.

Velocity Fields

Figure 7 illustrates the effect of radial injections on the jet boundary defined as the sonic surface, in RANS and ZDES2. In each picture, the controlled jet on the top is compared with the reference jet in the bottom. At a first glance, the mean flow given by RANS (top of the figure) and ZDES (middle) look very similar. One can see the impressive distortion caused by radial injections. The main difference is the length of the supersonic part in the controlled jet, this one being tremendously shortened in ZDES with respect to RANS. In addition, its lobes seem to be rapidly consumed in ZDES, whereas they last much longer in RANS. A priori, this aspect can be attributed to a more powerful turbulent diffusion in ZDES. One can also notice bulges and tightenings on the sonic surface of the reference jet as well as of the controlled one. They correspond, respectively, to the high- and low-velocity cells that result from the reflection of the inner expansion-compression fans on the jet boundary. From the third cell of the reference jet, the tightenings begin to be attenuated in RANS while they strengthen and persist further downstream in ZDES. The same remark holds for the controlled jet. This phenomenon is intuitively the opposite of the overdiffusion postulated for ZDES. On one hand, the radial diffusion of velocity is amplified in ZDES, and on the other hand, the propagation of supersonic waves inside the jet tube is better conserved. In RANS computations, the diffusion is explicitly introduced by the turbulent model, whereas in ZDES, the dynamics of the large eddies is explicitly calculated, making it possible to account for the interactions of the expansion/compression fans with the turbulent large vortices. Deeper investigations should be undertaken to understand these interactions. In addition, the period of the cells is reduced when the control is on. The bottom picture of Fig. 7 presents an instantaneous view of the sonic surface of both jets. It exhibits a striking disorganization of this surface which illustrates the strong action of fluctuating eddies and also makes the resemblance between the averaged jets obtained in RANS and ZDES even more surprising.

The axial-velocity field of the reference jet is displayed on Fig. 8 for the experiment (PIV), RANS, ZDES1, and ZDES2. The shock lens previously observed in Schlieren photographs can be seen again. Farther downstream, the PIV measurements reveal a row of round high-velocity cells due to the jet underexpansion. The RANS computation does not properly reproduce these patterns in spite of a first cell quite similar to the experimental one. On the contrary, both ZDES show very fair agreement with the experiment, the cells having the right circular shape and location. A close look at the stagnation pressure fields (not displayed here) reveals a central stream tube behind the shock lens enclosing a lower total pressure than that of the surrounding jet flow, indicating that the shock predicted by means of RANS method is slightly stronger in a small area around the jet axis. Consequently, the fluid particles, roughly subjected to the same pressure variations during their convection as the one of ZDES jets, reach the lowest pressures with lower peak velocities than in ZDES. This explains why the RANS cells are similar to round ones but with a velocity defect on the axis. However, the reflection and refraction of the expansion/compression fans against and inside the shear layer are probably to be taken into account. Moreover, the lower total pressure tube previously seen in the Schlieren pictures of the reference jet predicted by ZDES1 and ZDES2 is also noticed in Fig. 8 through a low-velocity spike on the jet axis. A closer look points out some discrepancies between ZDES1, on one hand, and, experiment and ZDES2 on the other hand.

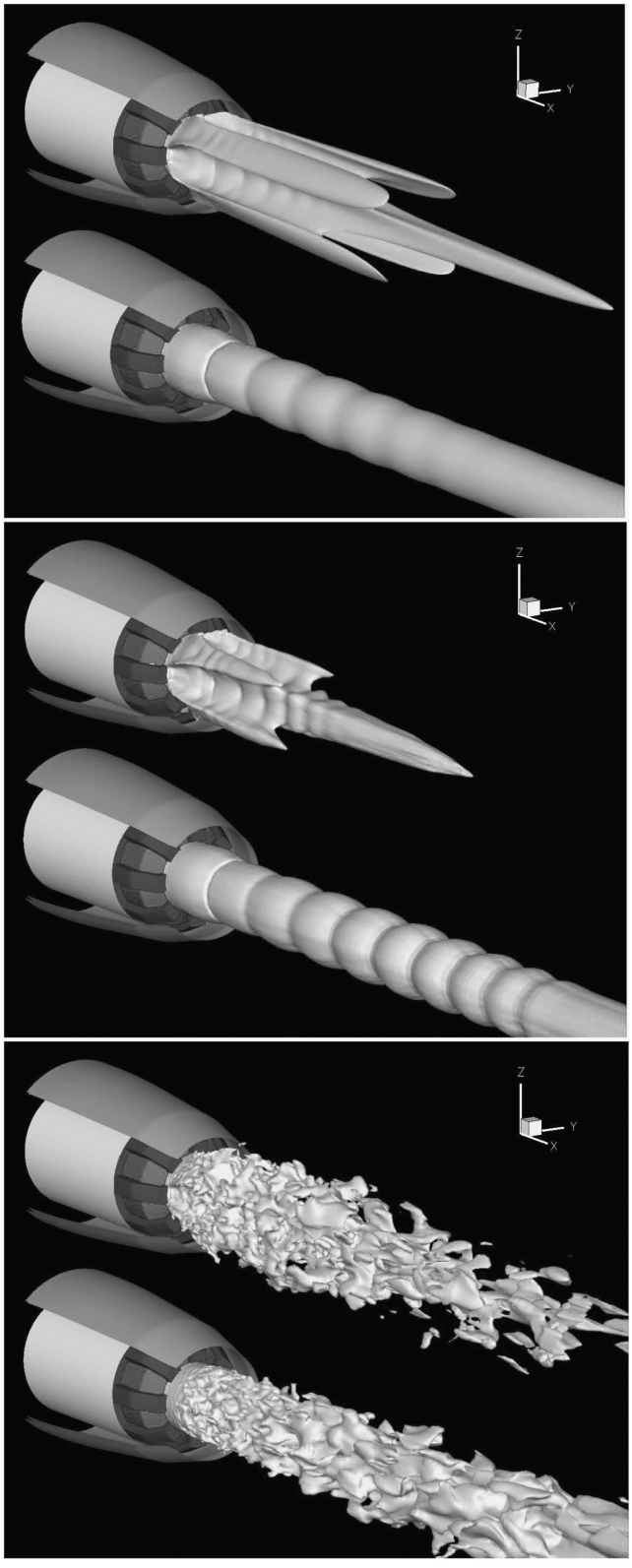

Fig. 7 Effect of four radial injections on the jet boundary (surface Mach = 1, reference jet in the bottom side, controlled jet in the upper side). Top: RANS; middle: ZDES 2 averaged view; bottom: ZDES 2 instantaneous view (grid M2).

Indeed, focusing on the first two cells, one can see that the shock is shifted downstream in ZDES1, which alters the wave propagation as illustrated by a different pattern at the end of the second cell: in experiment as well as in ZDES2, a concave low-velocity area is shown, whereas ZDES1 exhibits a triangular-shaped velocity distribution reflecting the occurrence of a straight conical compression-fan. It is known that PIV, because of seeding particle inertia, renders a shifted velocity field when this one has strong gradients. However, the overall topology of the velocity field is reliable. Then, even if the shock position can be questionable to distinguish between the two computations, the wave structure allows to show that ZDES2 better reproduce the flow field than ZDES1.

Longitudinal-velocity profiles are plotted in Fig. 9 for three probed axial positions, $X/D = 0.94|2.19|3.89$. The velocity is non-dimensionalized by the critical speed $a^* = 317\ \mathrm{m \cdot s^{-1}}$. In the reference jet (top of the figure), a rather fair agreement with the experiment is obtained with all the computations except ZDES1 at $X/D = 0.94$; see graph 9a. The velocity defect on the axis observed in experiment, RANS and ZDES2 is due to the intersection with the shock lens. This defect is not observed in the case of ZDES1 because the shock is located slightly more downstream. At $X/D = 3.89$, graph 9c, that is, in the fourth cell, one can notice the velocity defect on the axis of the RANS profile because of the lower stagnation pressure as explained above. The curves in the middle and bottom side of Fig. 9 show, respectively, the velocity profiles at the same abscissas for the controlled jet in an injection plane and an interplane. In this case, no significant distinction can be reported between the two ZDES results. An excellent correlation with experiment has here to be underlined which proves the capability of ZDES to reproduce the complex velocity diffusion taking place in a jet surrounded by eight macroscopic streamwise vortices. On the opposite, RANS profiles definitely distinguish themselves by sharp radial gradients, especially at $X/D = 3.89$; see graphs 9f and 9i. The lobes encountered in the top of Fig. 7 are evidenced by two outer velocity peaks on graph 9i, whereas the ZDES profiles are smoothed and show only the core velocity peak on the axis.

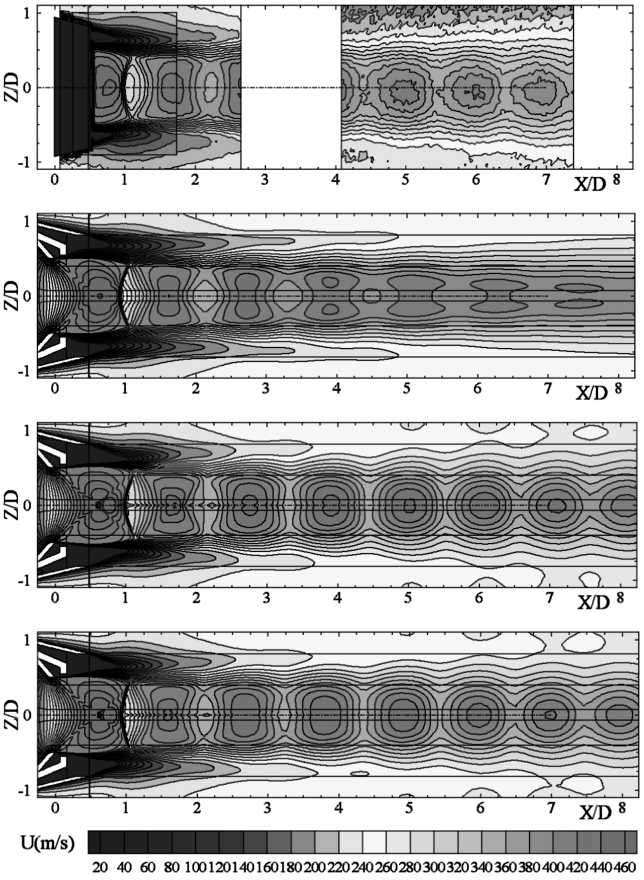

Fig. 8 Comparison of the axial-velocity fields (from top to bottom, experiment, RANS, ZDES 1, and ZDES 2 on grid M2).

Axial Pressures Behavior

Finally, both static and total pressures on the jet axis are plotted in Fig. 10 for the reference and controlled cases. They are nondimensionalized by the external stagnation pressure p_{i0}. In the reference jet, the static pressure oscillates around the level of the external pressure $p_0/p_{i0} = 0.66$. The surprising constant peak pressure downstream from the first shock is probably due to the shear alleviation induced by the external $M = 0.8$ coflow. This is not reproduced by RANS computations and a phase shift is also noticed. A better prediction of the pressure peaks is provided by ZDES methods even though a slight attenuation is still seen. ZDES1 differs from ZDES2 by a lower depression (low pressure peak) and a higher compression (high pressure peak) downstream of the first shock together with a strange pressure variation between these two extrema. This behavior corresponds to the triangular shape observed in the velocity field, Fig. 8. Besides, the stagnation pressure measured in the jet is lower than the one measured in the primary nozzle and adopted as inlet boundary condition in all the simulations RANS, ZDES1, and ZDES2. The imposed stagnation pressure was measured by a sensor fixed inside the nozzle and no additional measurements permit to assess a possible nonisentropic behavior between this sensor and the nearest probe location on the jet axis. Therefore, no explanation was found to understand this discrepancy in the total pressure. The step undergone by the RANS total pressure is an evidence of the stronger shock in the vicinity of the axis. All the displayed stagnation pressures are constant down to the edge of the probed region, that is $X/D = 5$, indicating that the jet potential core extends further downstream. When the radial injectors blow (see the experimental symbols in Fig. 10b) the static pressure oscillations reduce their wavelength and are quickly damped. This corroborates the behavior of the jet boundary described in Fig. 7. The experimental total pressure drops approximately from $X/D \approx 2.4$, which indicates the end of the potential core. This is also visible in Fig. 9 where, at $X/D = 2.19$, graphs 9e and 9h, the radial variations of velocity traduce the existence of inner waves, whereas, at $X/D = 3.89$, graphs 9f and 9i, the velocity profiles are smoothed, closer to a Gaussian function, consequently to the turbulent damping of the waves. All the computations qualitatively predict the wavelength shortening as well as the peak attenuation in the static pressure, and are quantitatively satisfactory. Looking at the total pressures, RANS overestimates the potential-core length to $X/D \approx 5.0$ while both ZDES give comparable results, $X/D \approx 2$, much closer to the measurements, $X/D \approx 2.4$, but rather optimistic for the control device.

Influence of the Grid Distribution in the Circumferential Direction

The effect of a reduction from 169 to 129 in the number of nodes in the azimuthal direction is now evaluated by comparing the axial pressures obtained, respectively, on grids M2 and M1 with both Δ definitions. It is also worth remembering that RANS computations gave exactly the same solution on both grids (see [13]). One can notice that the ZDES1 solution based on Δ_{vol}, Fig. 11a, is more dependent on the mesh size than the ZDES2 one which is based on Δ_ω, see Fig. 11b. Furthermore, this latter graph shows that ZDES2 with the finer mesh has almost reached the grid convergence relative to the azimuthal direction whereas it is not yet the case for ZDES1.

The whole set of data just presented clearly demonstrates the superiority of ZDES computations over RANS ones (at least for the Spalart–Allmaras model) for predicting the shear-layer mean properties of a geometrically and physically complex flow. Moreover, the new Δ definition proved to bring significant improvements at least in the initial portion of the shear layer and showed to be less sensitive to coarse circumferential grids than classical length scales. The next section will detail the effect of this modification on the intimacy of the shear layer and its large eddies.

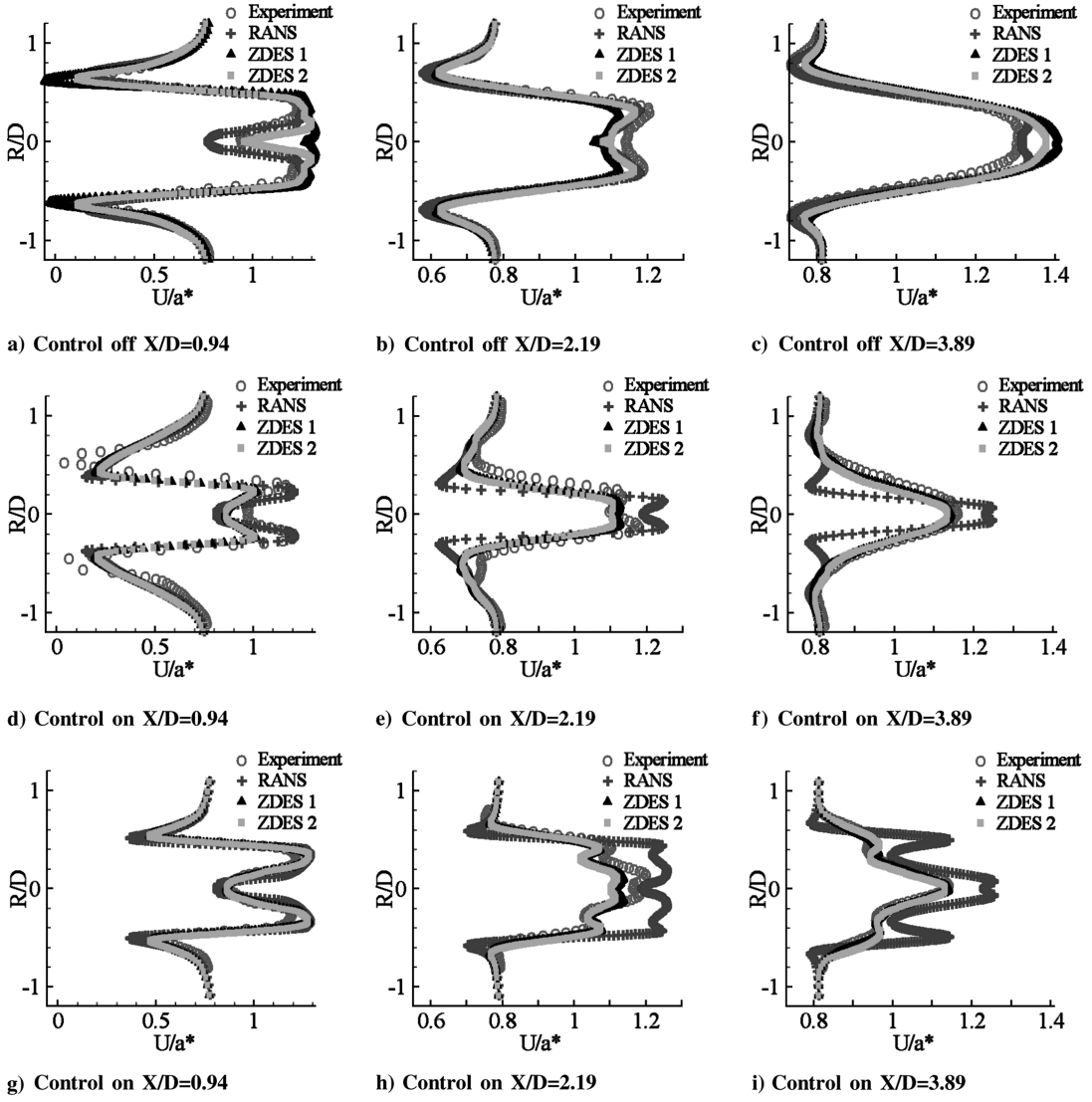

Fig. 9 Longitudinal-velocity u/a^* profiles in the uncontrolled (top) and controlled jet in the injection plane (middle) and in the interplane (bottom) on grid M2.

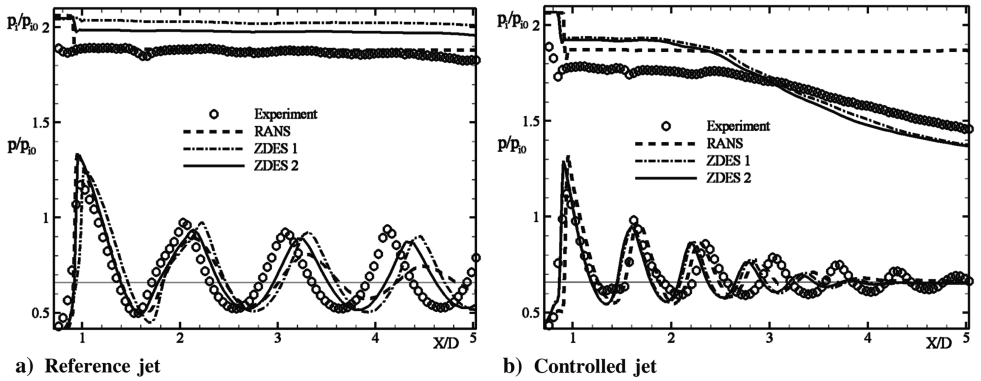

Fig. 10 Comparison of the axial pressures (grid M2).

Effect of the Modification of the Characteristic Length Scale Δ

The nondimensionalized Reynolds shear stress $\tau_{xr}^R/(\rho^* a^{*2})$ (ρ^* being the critical density) is plotted in Fig. 12 at $X/D = 0.48|2.19|3.89$, for the reference jet (top) and the controlled one, in injection-plane (middle) and in interplane (bottom). The Reynolds shear stress τ_{xr}^R is here defined as the sum of the modeled shear stress $\tau_{xr}^{\mathrm{RM}} = \tau_{xr}^d = 2\rho\nu_t S_{xr}$ and the resolved shear stress $\tau_{xr}^{\mathrm{RR}} = -\rho\langle u_x' u_r'\rangle$. In RANS curves, $\tau_{xr}^R = \tau_{xr}^{\mathrm{RM}}$ because no turbulence is resolved. On the opposite, in both ZDES, the resolved part makes up most of the Reynolds shear stress because, at $X/D = 2.19$, τ_{xr}^{RM} is only 0.3% of τ_{xr}^R. However, earlier at $X/D = 0.48$, $\tau_{xr}^{\mathrm{RM}}/\tau_{xr}^R$ is 2.4% in ZDES2, whereas in ZDES1, $\tau_{xr}^{\mathrm{RM}}/\tau_{xr}^R$ represents up to 68%. This means that, at this point, ZDES1 has not completely developed the shear-layer instability yet. Concomitantly, the shear-layer transition from a RANS layer to large eddies is delayed as seen in the instantaneous Schlieren pictures, Fig. 6. These values were extracted

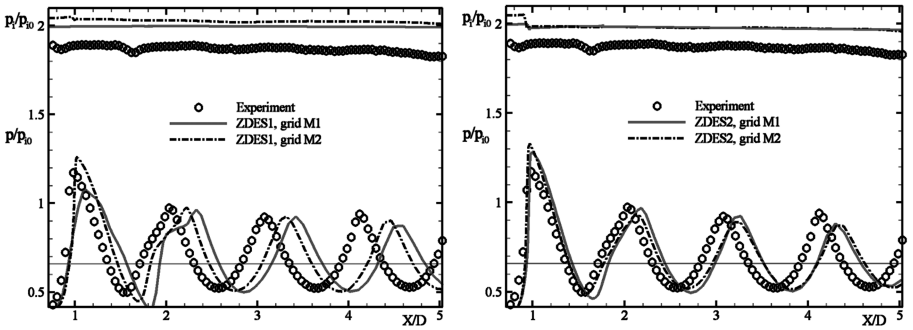

Fig. 11 Effect of the mesh on the axial pressures of the reference jet.

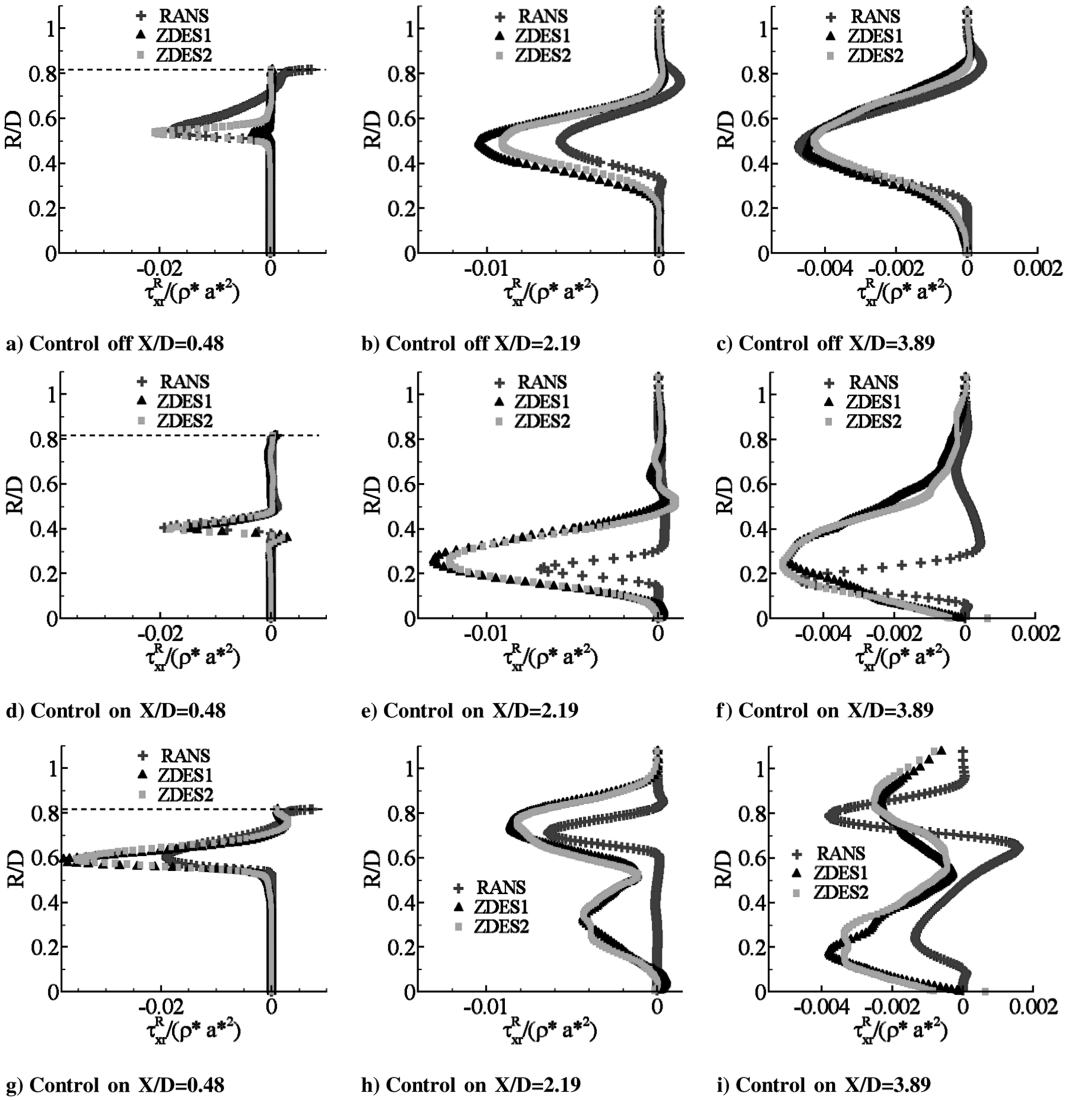

Fig. 12 Reynolds shear stress $\tau_{xr}^R/(\rho^* a^{*2})$ in the uncontrolled (top) and controlled jet in the injection plane (middle) and in the interplane (bottom) on grid M2.

from the reference jet. In the case of active injectors, the perturbations of the jet shear layer seem to be amplified, because, at the same abscissa, the portion of the modeled stress decreases in ZDES1, $\tau_{xr}^{\mathrm{RM}}/\tau_{xr}^R = 5.6\%$, and remains almost the same in ZDES2. As pointed out by the wave structure, in Fig. 8, the initial shear layer predicted by ZDES2 seems to be closer to the experiment than the one given by ZDES1. In Fig. 12a, we can see that τ_{xr}^R is much lower in ZDES1 than in ZDES2. Therefore, at $X/D = 0.48$, ZDES1 typically suffers from "modeled-stress depletion" [31], the fluctuations it generates are not yet powerful enough to compensate for the decrease in eddy viscosity. ZDES2, thanks to Δ_ω, decreased the value of its eddy viscosity earlier, and then lowered its modeled shear stress but in the same time allowed the resolved fluctuations to grow sufficiently and finally fulfill the LES content at $X/D = 0.48$. Farther downstream, the resolved parts of the shear stress in ZDES1 and ZDES2 become comparable and so do their Reynolds stresses; see graphs at $X/D = 2.19$ and 3.89. No significant distinction between the two ZDES can be seen either in the controlled case. Comparing RANS shear stress with the one provided by either one of ZDES computations from $X/D = 2$, we can globally conclude that the

turbulent shear is underpredicted as well as the transverse extent of the layer, although a surprising collapse can be noticed for the reference jet at $X/D = 3.89$. The general underestimation of the jet mixing, notably the potential-core lengths, is then an obvious outcome. In Fig. 12h, it is worth mentioning a peak of negative shear predicted by ZDES but not by RANS. This is the result of a faster disintegration of the lobes and of the fluid strips linking them to the central core of the jet as highlighted in Fig. 7. This disintegration occurs later in the RANS jet, then the peak appears farther downstream; see at $X/D = 3.89$, Fig. 12i.

To monitor the behavior of Δ_ω, the local components of the normalized vorticity $\boldsymbol{N}$, the value of 3 different Δ, and the resulting dynamic eddy viscosity μ_t normalized by the molecular viscosity are plotted in Fig. 13 for two locations, $X/D = 0.19$ and 1.52, in the mixing layer of the reference jet at an arbitrarily chosen time. The first one is characteristic of the very near field and the second one represents the fully developed turbulent shear layer. Let us begin in the near field. Figure 13a shows that the vortices highlighted in Fig. 6 are predominantly oriented in the spanwise direction z. As a result, Δ_ω was defined to be around $\sqrt{\Delta_x \Delta_y}$, and then adopts the smaller value of the Δ_ω field in coarse as well as in fine mesh sections. Thanks to the way the mesh has been built, this value is constant with respect to azimuth, as it can be checked in Fig. 13c. $\Delta_{\max}$ and Δ_{vol} are also plotted in this graph and are seen to be higher than the constant value of Δ_ω. Moreover, the values of $\Delta_{\max}$ and Δ_{vol} both depend on the azimuth through the azimuthal length scale Δ_z, whereas there is no physical justification for this. It is then not surprising to find the same trends in the μ_t values: ZDES2 exhibits a low-value constant eddy viscosity letting the resolved scales grow, whereas ZDES1 shows a higher eddy viscosity, freezing the shear layer, and also depending on the azimuth. Further downstream at $X/D = 1.52$, graph 13b, we can remark that the vorticity has no apparent preferred direction, even though a more rigorous statistical analysis should be performed to assess its probability distribution. Thereby, the value taken by Δ_ω fluctuates between the extreme values, $\sqrt{\Delta_y \Delta_z} \approx 4 \cdot 10^{-4}$ and $\sqrt{\Delta_z \Delta_x} \approx 1 \cdot 10^{-3}$, of the Δ_ω-field defined by (12). $\Delta_{\max}$ and Δ_{vol} are constant in azimuth thanks to the homogeneous mesh at this abscissa. The resulting eddy-viscosity values, plotted in graph 13f, show no significant difference as expected. These results better explain the invariance of ZDES2 with respect to the azimuthal length scale while ZDES1 is still dependent on the circumferential discretization. However, it is necessary to mention that a too strong

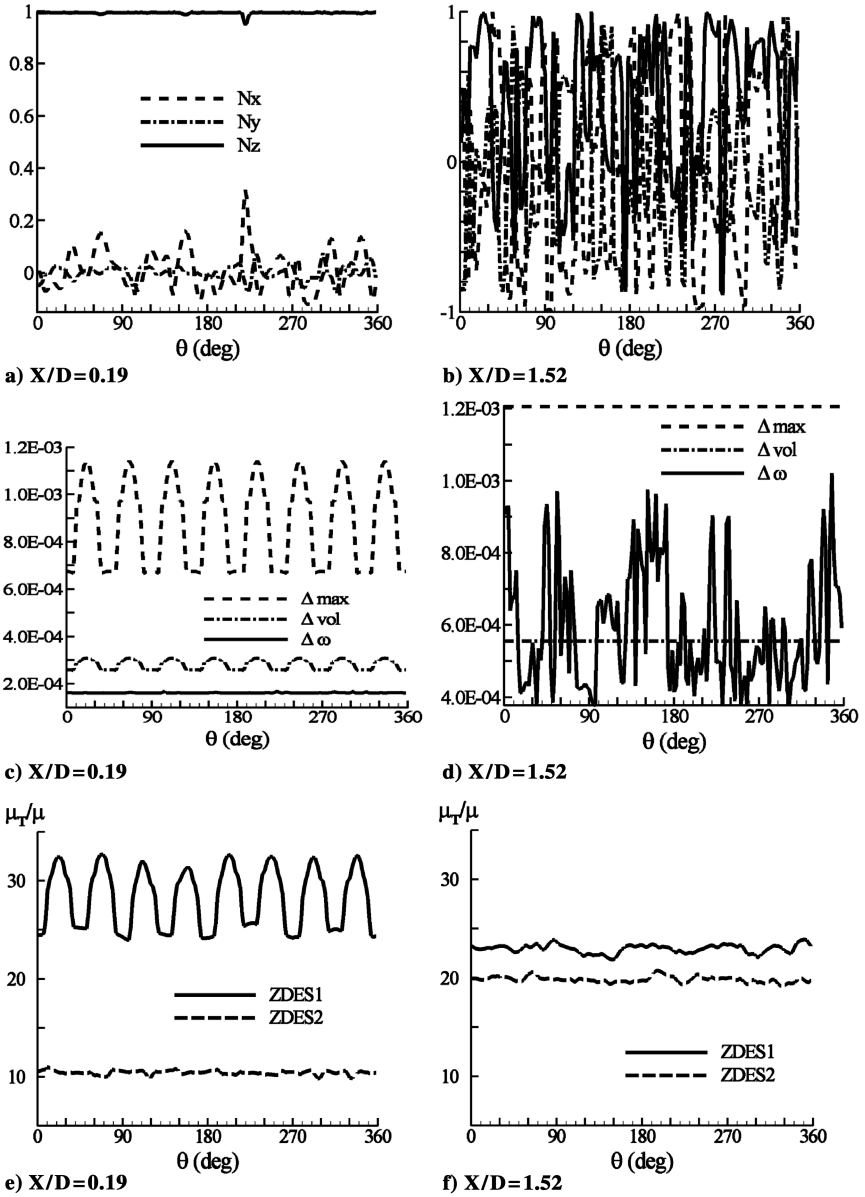

Fig. 13 Azimuthal variations in the components of the vorticity direction (top), $\Delta_{\max}$,Δ_{vol}, and Δ_ω (middle) and μ_T/μ (bottom) in two characteristic positions $X/D = 0.19$ (left) and $X/D = 1.52$ (right) of the mixing layer (control off). The azimuth is in degrees (results on grid M2).

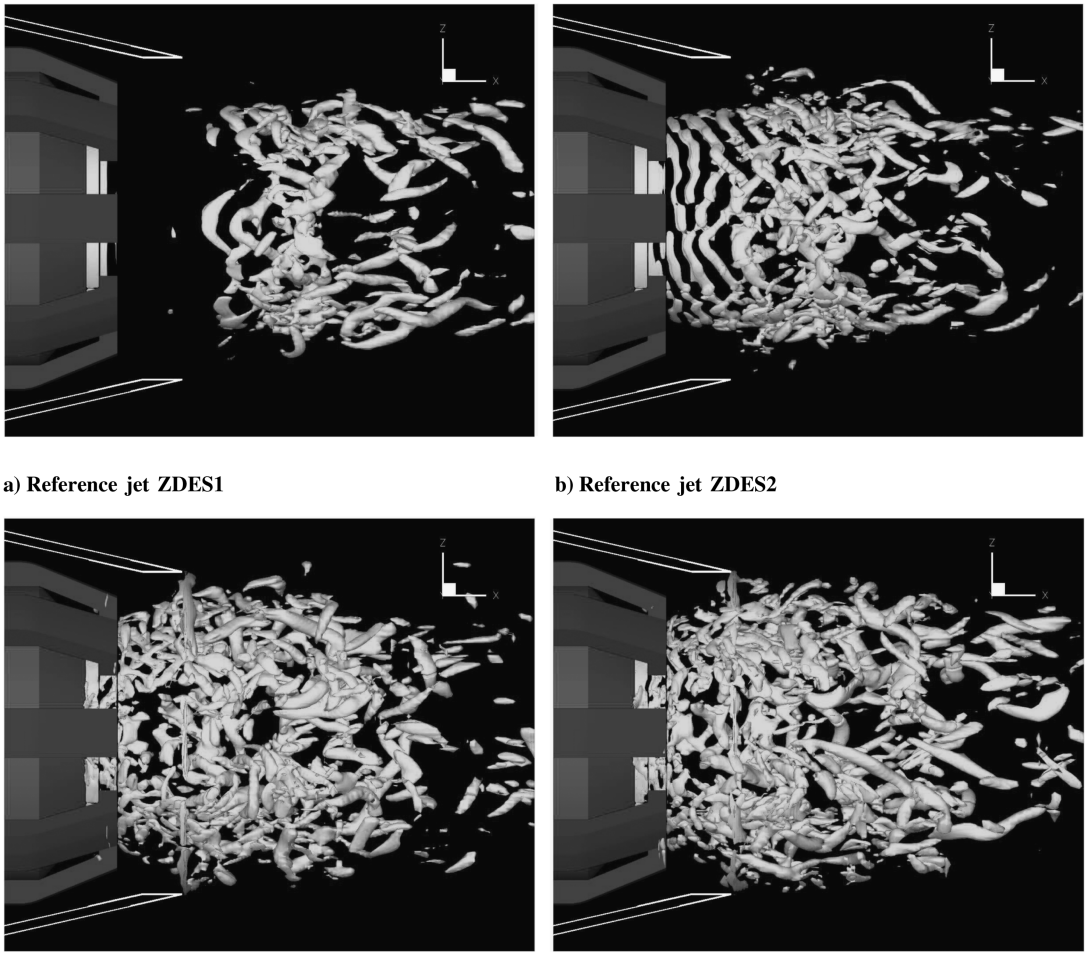

a) Reference jet ZDES1 b) Reference jet ZDES2

c) Controlled jet ZDES1 d) Controlled jet ZDES2

Fig. 14 Surfaces of constant Q criterion $[Q/(a^*/D)^2 = 50]$.

reduction of grid number in the circumferential direction will also alter the results of ZDES2 as soon as the vortical structures are not predominantly axisymmetric rollers.

Figure 14 illustrates the eddy structures in the very near field of the jet shear layer by means of the Q criterion [43]: $Q = \frac{1}{2}(\|\boldsymbol{\Omega}\|^2 - \|\mathbf{S}\|^2)$, for both ZDES. A value of $Q/(a^*/D)^2 = 50$ was chosen. Comparing Figs. 14a and 14b, the aforementioned delayed transition of the shear layer in ZDES1 is striking. From the nozzle throat to the end of the fairing, we can clearly count four rollers in ZDES2, whereas none can be seen in ZDES1. These rollers are nearly axisymmetric, though some particular oblique directions can be distinguished in this view. According to theoretical [44] and experimental studies [20], a plane shear layer begins to be sensitive to compressibility effects at around $M_c \approx 0.6$, which is the convective Mach number of the initial part of the jet shear layer studied here. It was shown [45] that the 2-D spanwise instability is the most amplified one until $M_c \approx 0.6$, and that above, oblique waves are the most amplified. A deeper investigation based on statistical analysis is necessary to conclude on the structure of the jet shear layer. Afterward, a rather messy vortical topology can be observed because of the unsteady recirculation bubble downstream of the ventilation channel and of the impact of the external coflow. The eddies seem to be more streamwise than at the very beginning. Downstream, the high-value of Q criterion can no longer capture the vortices which grow and concomitantly decrease their vorticity. When the secondary jets are blowing, the difference between ZDES1, Fig. 14c, and ZDES2, Fig. 14d, becomes less marked, as underlined above. The blowing directions are in the plane of the picture and normal to it. The effect of the control on the increasing number of vortical structures is obvious. Moreover, no nearly axisymmetric eddy can be detected, and streamwise vortices are more apparent than in the reference jet, especially in ZDES2.

Estimation of the Mixing Device Efficiency

Now that the computational method has been shown to correctly reproduce the test cases with control off and on, it is possible to probe the numerical fields to investigate the mixing process and assess the efficiency of the control device. Figure 15 compares the normalized-streamwise-vorticity fields $\Omega_x = (\boldsymbol{\nabla} \times \boldsymbol{u}) \cdot \boldsymbol{x} D/(2a^*)$ extracted from RANS, ZDES1, and ZDES2 computations of the controlled jet at $X/D = 1$ and 4. The lines of constant $p_i/p_{i0} = 1.05$ are also plotted for the controlled jet (thin line) and the reference jet (thick line) to bound the high-stagnation-pressure jet flow. From the beginning, the action of the radial injections and later of the resulting streamwise vortices is spectacular. Although the near fields are very similar, the subsequent evolution of the streamwise vortices is quite different in RANS and in both ZDES. As described in a former paper [13], the flow predicted by RANS calculation supports a scenario, highlighted by Zaman [46], according to which the streamwise vortices would penetrate the main jet in a first stage, and then would diverge from the central axis in a second stage, making the jet blow out. The jet fluid ejected from the central core in the form of four mushroom lobes is emphasized in Fig. 14d. These features are less apparent in the ZDES cross sections, Figs. 15e and 15f, and the magnitude of vorticity almost vanishes. To sum up, RANS calculation predicts long-life streamwise vortices, whereas ZDES suggest their rapid decay.

To verify which one of the two vortex evolutions is representative of the real flow, Fig. 16 compares the stagnation-pressure

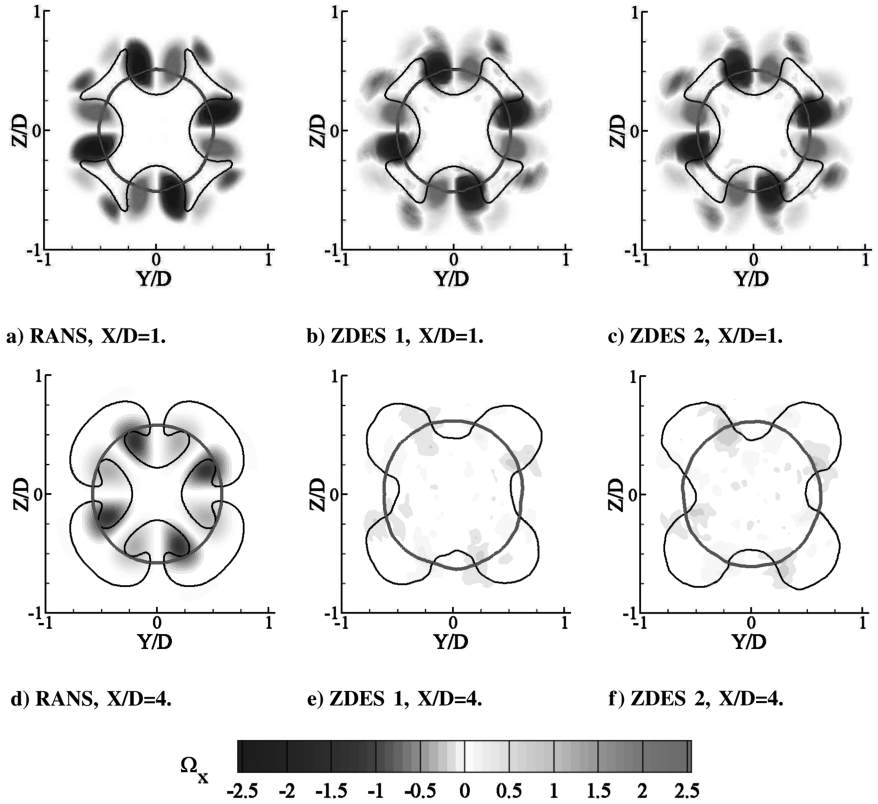

Fig. 15 Normalized-streamwise-vorticity contours, line $p_i/p_{i0} = 1.001$ controlled jet, four injections (thin line), line $p_i/p_{i0} = 1.05$ reference jet (thick circle).

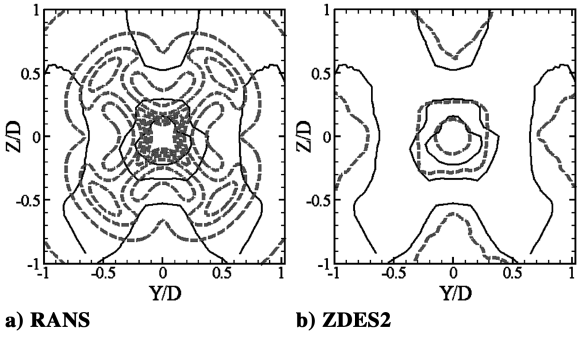

Fig. 16 Stagnation pressure in cross sections through the controlled jet at $X/D = 3.89$ (measurement, solid line; simulations, thick dashed line).

distributions given by RANS and ZDES2 to the one measured at $X/D = 3.89$. The lines p_i/p_{i0} are plotted every 0.2. ZDES results distinctly correlates the experiment, whereas RANS computation seems to underestimate the disintegration of the streamwise vortices. No mushroom lobes are visible either in the measured map. Thus, the assessment of the mixing efficiency of the control device is probably overestimated by RANS computations, at least in the far field.

Finally, the capability of the hypermixer is assessed. Some of the global measures of mixing proposed in [13] are used to evaluate the outcome of the mixing process. Their definitions are here briefly reminded. The jet volume is the volume of fluid in which the stagnation pressure is greater than $p_{i\text{ext}} = (0.95p_{i0} + 0.05p_{i1})$; it characterizes the expansion of the jet. The core volume is the fluid volume in which the stagnation pressure is greater than $p_{i\text{ext}} = 0.5(p_{i0} + p_{i1})$ and represents the higher-energy portion of the jet. These quantities were integrated in the range $0 \leq X/D \leq 9$. Concerning the reference jet and compared with RANS, ZDES2 (respectively ZDES1) forecasts a 14% (respectively 18%) greater jet volume, a smaller core volume by about 9% (respectively 7%), and a mean stagnation pressure lowered by 5% (idem for ZDES1). Globally, the mixing is then slightly greater in ZDES simulations. When the control is on, ZDES2 (respectively ZDES1) predicts an increase in jet volume V_j of about 44% (respectively 34%) and a decrease in core volume V_c of 69% (and ZDES1 also). The mean stagnation pressure of the fluid included in the jet volume $\langle p_i/p_{i0}\rangle$ is also reduced by 17% in both ZDES. Comparatively, RANS figures are the following: $\Delta V_j = +63\%$, $\Delta V_c = -51\%$, $\Delta\langle p_i/p_{i0}\rangle = -18\%$. It is a priori rather puzzling to notice that, compared with ZDES, RANS overestimates the jet volume, then the jet expansion, whereas it underestimates the core volume, and so the diffusion of the high-energy part of the jet. However, it would be awkward to extrapolate the RANS trends to ZDES because the ZDES method reproduces the dynamics of the large turbulent scales whereas the RANS method can only mimic a diffusive behavior. An estimation of the mixing activity of turbulence is provided by integrating the specific kinetic energy ρk, where $k = (\langle u'^2\rangle + \langle v'^2\rangle + \langle w'^2\rangle)/2$, from the nozzle exit $X/D = 0$ to $X/D = 9$. For the reference case, the integrated energy in the two ZDES only differs by less than 2%. The activation of the control leads to an increase in the global kinetic energy of 70%.

To follow the longitudinal evolution of the mixing process along the reference and controlled jets, the mean stagnation pressure in cross sections and the integrated specific turbulent kinetic energy are plotted in Fig. 17. This latter quantity is normalized by $\pi D^2 \rho^* a^{*2}/8$. In Fig. 17a, all the curves are decreasing, thus indicating the progressive dilution of stagnation pressure by turbulent mixing. No difference can be noticed between ZDES2 and RANS curves for the reference jet. ZDES1 distinguishes from the other computations in the very near field, by a lower drop of the mean stagnation pressure. This property is likely due to the delayed instability of the shear layer. In Fig. 17b, the kinetic energy quickly rises thanks to the instability growth of the shear layer and then decreases more gently because of the decay of the fully developed turbulence in the shear layer, the mean gradients vanishing as the flow progresses downstream. The shift between ZDES1 and ZDES2 curves supports the previous assumption on the effect of the delayed instability of ZDES1 shear layer. We can also mention that the kinetic energy mildly increases and decreases under the action of, respectively, compression waves

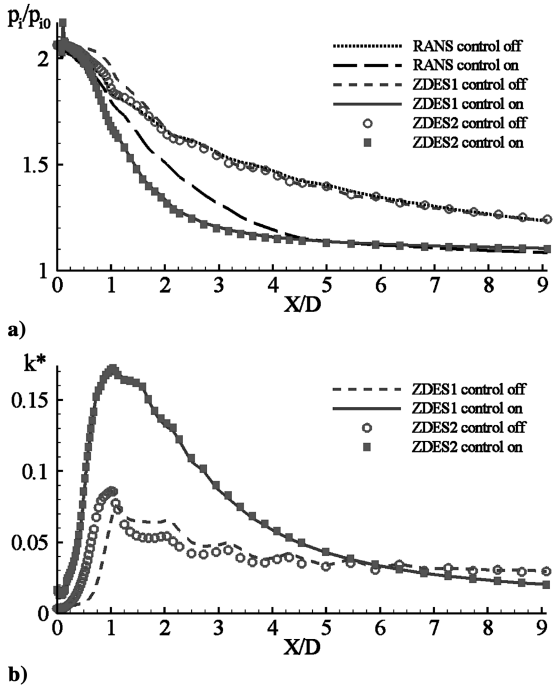

Fig. 17 a) Mean stagnation pressure p_i/p_{i0} and b) integrated turbulent kinetic energy k^* in cross sections along the jet axis.

and the expansion waves; see Fig. 8. This fact corroborates the longitudinal turbulent peaks due to shock/shear-layer impingement previously measured by Dash and Wolf [47]. When the injections blow, the stagnation pressure undergoes a dramatic drop in all the computations. As stated before, the differences are negligible between the two ZDES in this case. On the contrary, RANS total pressure shows a softer initial decrease which is, however, prolonged downstream because of the longer life of the streamwise vortices. Looking at Fig. 17b, we note that the turbulent energy peak in the controlled case is more than twice as high as the one of the reference jet, but later on, as the velocity gradients weaken more quickly, the turbulent motion cannot draw more energy from the mean flow and then dies faster than with no control.

Conclusions

The aim of the whole study was to investigate the mixing control of a realistic propulsive jet by radial sonic injections. This control device has proved efficient in canonical jets of former studies. Here, the challenge was to test it in an integrated generic flying-aircraft afterbody with all the geometrical and physical difficulties it implies. An experiment proved the action of such a device and asked for numerical computations to provide more extensive data to estimate the mixing efficiency more accurately and to enable a thorough understanding of the physical mechanisms involved. Such a complex simulation has been made possible thanks to the use of a zonal-DES approach that allows one to reduce the cost of the simulation by limiting the extent of the LES zones while maintaining the accuracy of URANS in the attached boundary layers. ZDES was shown to correctly reproduce the jet flowfield after approximately two nozzle diameters. As required by any LES-type simulation, special care has been devoted to mesh generation. However, owing to the geometrical complexity and due to the presence of shear layers, the cubic grids theoretically required are not yet affordable due to computing power limitations. Classical characteristic mesh lengths Δ employed in DES and ZDES lead to either an excessive stabilization of the flow or a delayed transition of the shear layer. Therefore, a new Δ definition was proposed to take into account the particular direction pointed by the instantaneous vorticity. Based on this new Δ, the ZDES method showed very fair agreement with experiment in both the near field and far field of the jet. In the controlled configuration, ZDES proved an accurate prediction of the streamwise vortices creation and subsequent decay. The computational method was finally judged satisfactory enough to perform a reliable evaluation of the mixing efficiency. The control device was shown both to increase the turbulent activity and to enhance the mixing dilution of the jet. The next step will be to understand the physical mechanisms leading to the improvement of the jet mixing and also those responsible for the rapid decay of longitudinal vortices.

References

[1] Spalart, P. R., "Strategies for Turbulence Modeling and Simulations," *International Journal of Heat and Fluid Flow*, Vol. 21, No. 3, 2000, pp. 252–263.

[2] Barber, T. J., Chiappetta, L. M., Debonis, J. R., Georgiadis, N. J., and Yoder, D. A., "Assessment of Parameters Influencing the Prediction of Shear Layer Mixing," *Journal of Propulsion and Power*, Vol. 15, No. 1, 1999, pp. 45–53.

[3] Dembowski, M. A., and Georgiadis, N. J., "An Evaluation of Parameters Influencing Jet Mixing Using the Wind Navier–Stokes Code," NASA TM-2002-211727, Aug. 2002.

[4] Georgiadis, N. J., Alexander, J. I. D., and Reshokto, E., "Hybrid Reynolds-Averaged Navier–Stokes/Large-Eddy Simulations of Supersonic Turbulent Mixing," AIAA J., Vol. 41, No. 2, 2003, pp. 218–229.

[5] Shur, M. L., Spalart, P. R., Strelets, M. K., and Garbaruk, A. V., "Further Steps in Les-Based Noise Prediction for Complex Jets," AIAA Paper 2006-485, 2006.

[6] Spalart, P. R., Jou, W. H., Strelets, M., and Allmaras, S. R., "Comments on the Feasibility of Les for Wings and on a Hybrid RANS/LES Approach," *Proceedings of the 1st U.S. Air Force Office of Scientific Research (AFOSR) International Conference on DNS/LES*, Greyden Press, Columbus, OH, 1997, pp. 137–147.

[7] Strelets, M., "Detached Eddy Simulation of Massively Separated Flows," AIAA Paper 01-0879, 2001.

[8] Constantinescu, G. S., and Squires, K. D., "Numerical Investigations of Flow over a Sphere in the Subcritical and the Supercritical Regimes," *Physics of Fluids*, Vol. 16, No. 5, 2004, pp. 1449–1466.

[9] Forsythe, J. R., Squires, K. D., Wurtzler, K. E., and Spalart, P. R., "Detached-Eddy Simulation of the F-15E at High Alpha," *Journal of Aircraft*, Vol. 41, No. 2, 2004, pp. 193–200.

[10] Molton, P., Jacquin, L., Chauvet, N., and Deck, S., "Mixing Enhancement in Under-Expanded Jet: Part 1," *Association Aeronautique et Astronautique de France Symposium on Applied Aerodynamics*, Association Aéronautique et Astronautique de France, Paris, March 2006.

[11] Davis, M. R., "Variable Control of Jet Decay," AIAA J., Vol. 20, No. 5, 1982, pp. 606–609.

[12] Collin, E., Barre, S., and Bonnet, J.-P., "Experimental Study of a Supersonic Jet-Mixing Layer Interaction," *Physics of Fluids*, Vol. 16, No. 3, 2004, pp. 765–778.

[13] Chauvet, N., Deck, S., and Jacquin, L., "Numerical Study of the Mixing Enhancement in a Supersonic Round Jet," *AIAA Journal*, Vol. 45, No. 7, 2007, pp. 1675–1687.

[14] Deck, S., "Numerical Simulation of Transonique Buffet over a Supercritical Airfoil," AIAA J., Vol. 43, No. 7, 2005, pp. 1556–1566.

[15] Deck, S., "Zonal Detached Eddy Simulation of the Flow Around a High-Lift Configuration," *AIAA Journal*, Vol. 43, No. 11, 2005, pp. 2372–2384.

[16] Shur, M. L., Spalart, P. R., and Strelets, M. K., "Noise Prediction for Increasingly Complex Jets, Part 1: Methods and Tests," *International Journal of Aeroacoustics*, Vol. 4, Nos. 3,4, 2005, pp. 213–246.

[17] Shur, M. L., Spalart, P. R., and Strelets, M. K., "Noise Prediction for Increasingly Complex Jets, Part II: Applications," *International Journal of Aeroacoustics*, Vol. 4, Nos. 3,4, 2005, pp. 247–266.

[18] Chauvet, N., Deck, S., Jacquin, L., and Molton, P., "Experimental-Numerical Investigation of Mixing Enhancement in Under-Expanded Jet," AIAA Paper 2006-4975, 9–12 July 2006.

[19] Bogdanoff, D. W., "Compressibility Effects in Turbulent Shear Layers," AIAA J., Vol. 21, No. 6, 1983, pp. 926–927.

[20] Papamoschou, D., and Roshko, A., "The Compressible Turbulent Shear Layer: An Experimental Study," *Journal of Fluid Mechanics*, Vol. 197, Dec. 1988, pp. 453–477.

[21] Ghosal, S., and Moin, P. J., "Large Eddy Simulation in Complex Geometry," *Journal of Computational Physics*, Vol. 118, No. 1, 1995, pp. 24–37.

[22] Péchier, M., "Prévisions Numériques de l'Effet Magnus pour des Configurations de Munition," Ph.D. Thesis, Department of Mechanical

Engineering, Univ. de Poitiers, Poitiers, France, Sept. 1999.
[23] Péchier, M., Guillen, P., and Caysac, R., "Magnus Effect over Finned Projectiles," *Journal of Spacecraft and Rockets*, Vol. 38, No. 4, 2001, pp. 542–549.
[24] Deck, S., Duveau, P., d'Espiney, P., and Guillen, P., "Development and Application of Spalart Allmaras One Equation Turbulence Model to 3-D Supersonic Complex Configurations," *Aerospace Science and Technology*, Vol. 6, No. 3, 2002, pp. 171–183.
[25] Larchevêque, L., "Large-Eddy Simulation of a Compressible Flow Past a Deep Cavity," *Physics of Fluids*, Vol. 15, No. 1, 2003.
[26] Simon, F., Deck, S., Guillen, P., and Sagaut, P., "Reynolds-Averaged Navier–Stokes/Large-Eddy Simulations of Supersonic Base Flow," *AIAA Journal* (to be published).
[27] Dandois, J., Garnier, E., and Sagaut, P., "Unsteady Simulation of a Synthetic Jet in a Crossflow," *AIAA Journal*, Vol. 44, No. 2, 2006, pp. 225–238.
[28] Spalart, P. R., and Allmaras, S. R., "A One Equation Turbulence Model for Aerodynamics Flows," AIAA Paper 92-0439, 1992.
[29] Spalart, P. R., and Allmaras, S. R., "A One Equation Turbulence Model for Aerodynamics Flows," *La Recherche Aérospatiale*, Vol. 1, 1994, pp. 5–21.
[30] Spalart, P. R., "Young-Person's Guide to Detached-Eddy Simulation Grids," NASA CR-2001-211032, July 2001.
[31] Spalart, P. R., Deck, S., Shur, M. L., Squires, K. D., Strelets, M. K., and Travin, A., "A New Version of Detached-Eddy Simulation, Resistant to Ambiguous Grid Densities," *Theoretical and Computational Fluid Dynamics*, Vol. 20, 2006, pp. 181–195.
[32] Breuer, M., Jovicic, N., and Mazaev, K., "Comparison of DES, RANS and LES for the Separated Flow Around a Flat Plate at High Incidence," *International Journal for Numerical Methods in Fluids*, Vol. 41, 2003, pp. 357–388.
[33] Sagaut, P., Deck, S., and Terracol, M., *Multiscale and Multiresolution Approaches in Turbulence*, Imperial College Press, London, 2006.
[34] Deardorff, J. W., "A Numerical Study of Three-Dmensional Turbulent Channel Flow at Large Reynolds Numbers," *Journal of Fluid Mechanics*, Vol. 41, 1970, pp. 453–465.
[35] Scotti, A., and Meneveau, C., "Generalized Smagorinsky Model for Anisotropic Grids," *Physics of Fluids*, Vol. 5, No. 9, 1993, pp. 2306–2308.
[36] Shur, M. L., Spalart, P. R., Strelets, M. K., and Travin, A., "Detached-Eddy Simulation of an Airfoil at High Angle of Attack," *Proceedings of the 4th International Symposium on Engineering Turbulence Modelling and Experiments*, edited by W. Rodi and D. Laurence, Elsevier, Corsica, 1999.
[37] Wallace, D., and Redekopp, L. G., "Linear Instability Characteristics of Wake-Shear Layers," *Physics of Fluids*, Vol. 4, No. 1, 1992, pp. 189–191.
[38] Georgiadis, N. J., Rumsey, C. L., Yoder, D. A., and Zaman, K. B. M. Q., "Turbulence Modeling Effects on Calculation of Lobed Nozzle Flowfields," *Journal of Propulsion and Power*, Vol. 22, No. 3, 2006, pp. 567–575.
[39] Payne, J. L., Roy, C. J., and Beresh, S. J., "A Comparison Of Turbulence Models for a Supersonic Jet in Transonic Crossflow," AIAA 2001-1048, 2001.
[40] Dacles-Mariani, J., Zilliac, G. G., Chow, J. S., and Bradshaw, P., "Numerical-Experimental Study of a Wingtip Vortex in the Near Field," *AIAA Journal*, Vol. 33, No. 9, 1995, pp. 1561–1568.
[41] Rylov, A. I., "On the Impossibility of Regular Reflection of a Steady-State Shock Wave from the Axis of Symmetry," *Journal of Applied Mathematics and Mechanics*, Vol. 54, No. 2, 1990, pp. 200–203.
[42] Zaman, K. B. M. Q., "Spreading Characteristics of Compressible Jets from Nozzles of Various Geometries," *Journal of Fluid Mechanics*, Vol. 383, 1999, pp. 197–228.
[43] Jeong, J., and Hussain, F., "On the Identification of a Vortex," *Journal of Fluid Mechanics*, Vol. 285, 1995, pp. 69–94.
[44] Blumen, W., "Shear-Layer Instability of an Inviscid Compressible Fluid," *Journal of Fluid Mechanics*, Vol. 40, 1970, pp. 769–781.
[45] Sandham, N. D., and Reynolds, W. C., "Compressible Mixing Layer: Linear Theory and Direct Simulation," *AIAA Journal*, Vol. 28, No. 4, 1990, pp. 618–624.
[46] Zaman, K. B. M. Q., "Axis Switching and Spreading of an Asymmetric Jet: The Role of Coherent Structure Dynamics," *Journal of Fluid Mechanics*, Vol. 316, 1996, pp. 1–27.
[47] Dash, S. M., and Wolf, D. E., "Interactive Phenomena in Supersonic Jet Mixing Problems, Part 2: Numerical Studies," AIAA J., Vol. 22, No. 10, 1984, pp. 1395–1404.

D. Gaitonde
Associate Editor